

High-entropy transition metal nitride thin films alloyed with Al: Microstructure, phase composition and mechanical properties

A.V. Pshyk^{a,b,c,*}, A. Vasylenko^d, B. Bakht^b, L. Hultman^b, P. Schweizer^c, T.E.J. Edwards^c, J. Michler^c, G. Greczynski^b

^a NanoBioMedical Centre, Adam Mickiewicz University, Poznań, Poland

^b Thin Film Physics Division, Department of Physics (IFM), Linköping University, SE-581 83 Linköping, Sweden

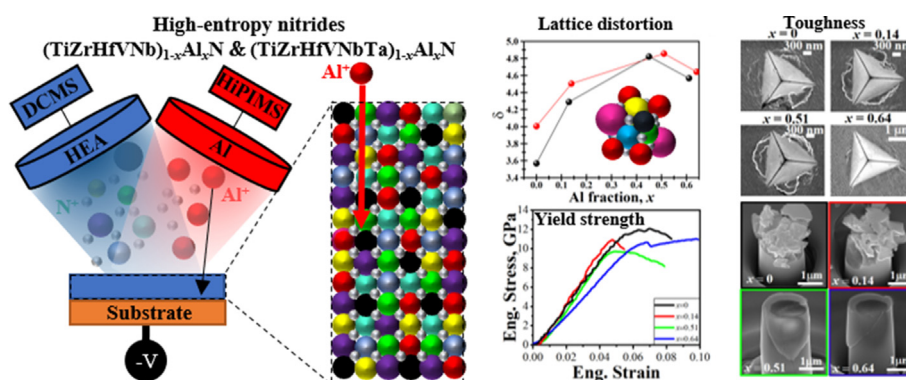
^c Empa – Swiss Federal Laboratories for Materials Testing and Research, Laboratory for Mechanics of Materials and Nanostructures, Thun CH-3602, Switzerland

^d Department of Chemistry, University of Liverpool, Liverpool, United Kingdom

HIGHLIGHTS

- (TiHfNbVZr)_{1-x}Al_xN and (TiHfNbVZrTa)_{1-x}Al_xN high-entropy nitride thin films are synthesised utilizing a hybrid PVD method.
- The hexanary and heptanary thin films are based on single-phase fcc-NaCl structured solid solution.
- Al concentration in high-entropy nitride thin films determines hardness, yield strength, toughness, and plasticity.
- The solid solution is stable up to $x \sim 0.51$ – 0.61 and up to $x \sim 0.45$ – 0.64 for the hexanary and heptanary films, respectively.
- Mechanical properties are determined by deformation mechanisms arising from the electronic structure and phase composition.

GRAPHICAL ABSTRACT



ARTICLE INFO

Article history:

Received 2 May 2022

Revised 25 May 2022

Accepted 27 May 2022

Available online 30 May 2022

Keywords:

High-entropy nitride

HiPIMS

Mechanical properties

Hardness

Yield strength

ABSTRACT

Deviation from equimolar composition in high-entropy multielement ceramics offers a possibility of fine-tuning the materials' properties for targeted application. Here, we present a systematic experimental and theoretical study on the effects of alloying equimolar pentanary (TiHfNbVZr)N and hexanary (TiHfNbVZrTa)N high-entropy nitrides with Al. Although being predicted to be metastable by ab initio density-functional theory calculations, single-phase fcc NaCl-structured solid solution thin films with Al solubility limits as high as $x \sim 0.51$ – 0.61 in (TiHfNbVZr)_{1-x}Al_xN and $x \sim 0.45$ – 0.64 in (TiHfNbVZrTa)_{1-x}Al_xN are synthesised utilizing a hybrid deposition technique that offers dynamic mixing of film atoms from Al⁺ subplantation and non-equilibrium growth conditions leading to quenching of the desired film structure. In experimental studies supplemented with density-functional theory calculations, it is demonstrated that Al concentration in alloys with the multielement compositions of high-entropy nitride thin films determine hardness, yield

* Corresponding author.

E-mail address: oleksandr.pshyk@liu.se (A.V. Pshyk).

strength, toughness, and ability to deform plastically up to fracture due to different deformation mechanisms arising from the electronic structure and phase compositions.

© 2022 The Author(s). Published by Elsevier Ltd. This is an open access article under the CC BY license (<http://creativecommons.org/licenses/by/4.0/>).

1. Introduction

Transition metal nitride (TMN) thin films exhibit extraordinary properties due to the unique mixture of metallic, ionic, and covalent chemical bondings that determine their applicability in wide-ranging technologies [1,2]. Continuous search for innovative material solutions with advanced properties via multicomponent alloying has led to a relatively novel alloying material design concept, initially termed as “high-entropy alloys” (HEAs) [3]. According to the original theory, being composed of at least five principal elements in equiatomic (or close to equiatomic) amounts, the maximum configuration entropy stabilize them into a single-crystal solid-solution phase against the formation of the thermodynamically competing intermetallic phases. It is generally accepted that the configuration entropy becomes significant in HEAs and overcomes the enthalpy term contributing to stabilization of a solid solution through minimization of Gibbs free energy of mixing when reaching $1.5R$ (R is the universal gas constant) that exclude alloys with fewer than 5 components [4]. Ultimately, the high-entropy concept has been extended into the field of ceramics including TMNs. Recently, high-entropy transition metal nitrides (HENs) have emerged as promising candidates for the advancement of next generations of TMN-based thin films [5]. In analogy to HEAs, multicomponent nitrides composed of at least five principal binary nitrides are typically defined as HENs. NaCl-structured HENs are composed of chemically disordered metal and chemically ordered non-metal sublattices, hence, only metal sublattice contributes to their configuration entropy of $\geq 1.5R$ [6]. HENs have gained considerable interest in the scientific community, demonstrating a mixture of properties, often highly enhanced in comparison to the conventional TMN counterparts [5]. Extensive studies have been performed focusing mostly on the investigation of the dependence of the structural and mechanical properties of HENs on varying the deposition parameters of PVD processes such as reactive gas flow, substrate bias potential, and substrate temperature [7,8]. However, a vast compositional space and lack of the systematic studies of their functional properties, limits their introduction to applications. Moreover, the majority of studies have been devoted to the HENs with maximum configuration entropy [7], i.e., equimolar compositions, while the hyper-dimensional composition space of non-equimolar HENs remains largely unexplored, limiting realization of a significant potential from both economical point of view and emerging functional properties.

Simultaneous improvement of both hardness and ductility, i.e. toughness, is a long-standing challenge in the field of TMNs [9]. It has been theoretically and experimentally demonstrated that the mechanical properties of binary and ternary transition metal nitrides can be effectively tuned by varying valence electron concentration (VEC) per unit cell [10]. Following this direction, HENs offer opportunities via VEC adjustment due to the vast space for compositional variations. Another phenomenon determining the mechanical properties of HEAs is lattice distortion originating from large differences in the size of component atoms. These effects have not been systematically investigated for HENs.

Alloying of TMNs with Al have shown an improvement of mechanical, functional, and thermal properties provided that the partial substitution of the TM by Al in the B1, NaCl structure does not exceed a solubility limit, and, hence, the precipitation of thermodynamically favored yet softer w-AlN phase is avoided [11]. Although, the solubility of Al in TMNs at thermodynamic

equilibrium is extremely low, it can be considerably extended under nonequilibrium growth conditions offered by PVD methods (such as magnetron sputtering or cathodic arc deposition) resulting in metastable supersaturated NaCl-structured solid solutions. Therefore, alloying of TMNs with maximum possible Al content while retaining single-phase NaCl-structured solid solution is among the challenges in the field of Al-containing TMN.

It is recently demonstrated that a relatively novel hybrid approach based on combining metal-ion synchronized high power impulse magnetron sputtering (HiPIMS) and direct current magnetron sputtering (DCMS) allows to increase Al solubility limit in TMNs, in particular in TiAlN [12], ZrAlN [13], and VAlN [14] up to the theoretically predicted values, in comparison to the solubility limits reached by the conventional PVD methods. Therefore, the hybrid HiPIMS/DC co-sputtering method is used in this work.

Here, we present a study on high-entropy transition metal nitride thin films based on pentanary $(\text{TiHfNbVZr})_{1-x}\text{Al}_x\text{N}$ and hexanary $(\text{TiHfNbVZrTa})_{1-x}\text{Al}_x\text{N}$ alloys with Al content x varying from 0 to ~ 0.6 . Al is selected as the alloying element in this study because it is critical for improving a wide range of mechanical, functional and thermal properties of TM-based nitrides [15]. Layers are deposited using a co-sputtering approach that combines HiPIMS from an Al target and DCMS from high-entropy alloy targets, i.e., TiHfNbVZr and TiHfNbVZrTa. A negative substrate bias is synchronized with the Al-rich portion of the HiPIMS pulse for an effective Al subplantation [12]. Varying the Al content in the two different series of films provides a systematic change in the lattice distortion (δ) and VEC and allows us to study the impact of Al concentration, δ and VEC on the microstructure, phase composition, and mechanical properties of the HEN films. Configuration entropy calculation for the two systems gives values that satisfy criteria for high-entropy materials thus supporting that the studied material is truly HEN. In order to provide insights into the microstructure and phase composition of HENs with different Al content a wide range of complementary analytical methods and techniques are utilized. We evaluate perspectives of HENs by investigating a wide range of mechanical properties such as hardness, elastic modulus, yield stress, and toughness. Trends in mechanical properties are determined and discussed in relation to the microstructure, phase composition, lattice distortion, and valence electron concentration of the HENs.

2. Experimental details

HEN thin films are grown in an industrial CemeCon AG CC800/9 magnetron sputtering system, equipped with HiPIMS and DC magnetrons. The films are deposited using elemental target of Al (CemeCon AG, Germany) and compound targets based on five and six transition metals, TiHfZrNbV and TiHfZrNbVTA, respectively, with dimensions $8.8 \times 50 \text{ cm}^2$. The compound targets are produced using spark plasma sintering method by PLANSEE AG, Germany. The deposition system is degassed for 2 h before deposition at a temperature of about 500°C using resistive heaters mounted symmetrically on the front and back sides of the vacuum chamber. All films are deposited at a substrate temperature of 450°C . The system base pressure is lower than $\sim 0.3 \text{ mPa}$, and the total pressure during deposition is $\sim 0.5 \text{ Pa}$ with a $\text{N}_2/(\text{N}_2 + \text{Ar})$ flow ratio of ~ 0.18 . The target-to-substrate distance is 18 cm. Single-crystal Si(001) and $\text{Al}_2\text{O}_3(0001)$ substrates are mounted symmetrically with respect to the targets forming a 21° angle between the substrate normal

and the normal to the target (see [Supplementary Fig. S1](#)). The substrates are ultrasonically cleaned in acetone and isopropanol for 10 min prior to loading to the chamber.

Two series of HEN thin films with different Al fraction on the metal sublattice $x = \text{Al}/(\text{TM} + \text{Al})$ are grown. The first series is based on $(\text{TiHfZrNbV})\text{N}$, while the second on $(\text{TiHfZrNbV}\text{Ta})\text{N}$. The compound targets are operated in the DC mode, while the Al target is powered by HiPIMS (i.e. Al-HiPIMS/HEA-DCMS). Al-free films are also grown as reference. The average HiPIMS and DC powers are varied in order to obtain different Al content in the film while keeping the deposition rate and the target current density in the same range for the films from different series with similar Al content (see [Supplementary Table 1](#)). HiPIMS pulse length is set to 100 μs and the pulsing frequency is varied from 200 to 600 Hz at different HiPIMS power in order to keep the target current density in the range 0.51–0.57 A/cm^2 (see [Supplementary Fig.S2](#) and [Supplementary Table 1](#)). A pulsed substrate bias of -60 V is applied synchronously with the Al-HiPIMS pulses with the pulse length of 100 μs and an offset of 30 μs in order to act on the metal-rich portion of the ion flux arriving at the substrate. The offset and the pulse length are previously determined for Al target by time-resolved ion-mass spectrometry measurements [16]. Between the HiPIMS pulses, the substrate is at floating potential (-20 V). The deposition time is varied from 43 to 60 min to attain $\sim 3\text{ }\mu\text{m}$ thick films. The film growth rate is estimated from the cross-sectional SEM images.

The phase composition and crystal structure of the HEN thin films are determined using Bragg-Brentano X-ray diffraction (XRD) using a PANalytical Empyrean X-ray diffractometer with $\text{Cu K}\alpha$ radiation ($\lambda = 0.15406\text{ nm}$) operated at 45 kV and 40 mA. θ - 2θ X-ray diffraction scans as a function of the sample tilt angle ψ is carried for more accurate phase determination in a Philips X'Pert MRD system with point-focus $\text{Cu K}\alpha$ radiation source operated at 45 kV and 40 mA. The tilt angles ψ used are 0° , 18.4° , 26.6° , 33.2° , 39.2° , 45.0° , 50.8° , 56.8° , 63.4° , and 71.6° . Residual stresses of the films are calculated using Stoney's equation and the substrate curvature is determined by rocking curve measurements of Al_2O_3 (0012) reflections in a Panalytical Empyrean XRD system. The microstructure and thickness of the HEN thin films are determined from fracture cross-section images obtained using a Zeiss LEO 1550 scanning electron microscope (SEM).

The composition and stoichiometry of HEN films are determined by X-ray photoelectron spectroscopy (XPS) and time-of-flight elastic recoil detection analysis (ToF-ERDA). The elemental compositions of the films are first obtained by ToF-ERDA carried out in a tandem accelerator with a 36 MeV $^{127}\text{I}^{8+}$ probe beam. More details about the measurements and analyses are given in reference [17]. Due to the limited mass resolution for heavy recoils, there are overlaps between signals coming from Ti and V, Zr and Nb, and Hf and Ta. Thus, the sum of Ti/V, Zr/Nb, and Hf/Ta concentrations is determined by ToF-ERDA. Then, the reliable ratios of heavy elements are obtained by XPS, which are also examined using EDS coupled to the SEM equipment. The chemical bonding of the films is evaluated by XPS using a Kratos Axis Ultra DLD instrument that employs Al $\text{K}\alpha$ radiation ($h\nu = 1486.6\text{ eV}$). The base pressure during spectra acquisition is $1.5 \times 10^{-7}\text{ Pa}$. Prior to spectra acquisition, all films are first sputter-etched for 120 s with a 4 keV Ar^+ ion beam incident at 70° with respect to the sample normal. The Ar^+ ion energy is then reduced to 0.5 keV for 600 s to minimize surface damage. The analyzed area has a size of $0.3 \times 0.7\text{ mm}^2$ and is centered in the middle of the $3 \times 3\text{ mm}^2$ etched area. The binding energy scale is calibrated by examining the sputter-cleaned Au, Ag, and Cu samples according to the recommended ISO standards for monochromatic Al $\text{K}\alpha$ sources that place Au $4f_{7/2}$, Ag $3d_{5/2}$, and Cu $2p_{3/2}$ peaks at 83.96, 368.21, and 932.62 eV respectively [18]. The Fermi edge, clearly observed for all layers, is set as "0 eV" after fitting by the "Step Down"

background type in Case XPS and used as the charge reference [19]. XPS spectra quantification and deconvolution is performed using CasaXPS software package. Transition metal core level spectra are fitted using constraints for the area ratio of spin-orbit split doublets as 0.5, 0.666 and 0.75 for Ti 2p and V 2p, Nb 3d and Zr 3d, Hf 4f and Ta 4f, respectively. The same constraints are applied to corresponding satellite peaks. No constraints are used for FWHM and the binding energy.

Raman spectroscopy is performed using Renishaw inVia confocal Raman microscope with 633 nm laser radiation. Spectra are recorded at laser power 50% with 8–9 accumulations and exposition time was set to 10.00 s.

The composition data and XRD lattice parameter are used for calculating the lattice distortion parameter (δ , %), configuration entropy (S_{conf}) at the metal sub-lattice and valence electron concentration per formula unit (VEC, $e^-/\text{f.u.}$). The details are given in [Supplementary Note 1](#).

Transmission electron microscopy (TEM) investigations are performed using a probe-corrected Thermo Scientific Titan Themis 200 G3 operated at 200 keV. Energy dispersive X-ray spectroscopy is acquired with the integrated SuperX detector.

Samples for imaging and elemental analysis by TEM and EDS are prepared by focused ion beam (FIB) using the FIB lift out method, in a FEI Helios NanoLab G3 UC Dual Beam SEM/Ga-FIB system, with a protective layer applied by electron- and ion-beam assisted gas deposition, and thinning of the lamella down to 30 kV, 30 pA. Final polishing for high resolution imaging was carried out at 5 kV 25 pA, and then 2 kV 50 pA.

The nanoindentation is performed to measure hardness and Young's modulus of the films using an Ultra-Micro Indentation System indenter equipped with a Berkovich diamond probe. At least 36 indents are performed on each sample at fixed load satisfying the condition that the penetration depth is less than 10% of the film thickness. The Poisson's ratio required for calculation of the Young's modulus is estimated following the rule of mixture of constituting binary nitrides. Nanoindentation toughness is estimated by performing at least 4 indents on each sample with a cube-corner diamond tip over a load range from 80 to 500 mN [20].

Micropillar compression is performed *in situ* in a Zeiss DSM 962 SEM using an Alemnis *in situ* indenter equipped with a 5 μm wide flat punch diamond tip. At least 3–4 pillars are compressed for each film. Micro-pillars are fabricated using Ga^+ ion beam milling at an accelerating voltage of 30 kV in a Tescan Vela instrument. The milling ion current is stepwise reduced from 5 nA (coarse milling) to 100 pA (fine milling) in order to minimize irradiation damage. The final taper angle of the pillars does not exceed 3° . Considering the small taper angle of the pillars, the pillar diameter at the middle of the pillar height is used for the stress calculations. The pillars are all fabricated with equivalent diameter of $\sim 1.8\text{ }\mu\text{m}$ and are milled down until the film/substrate interface; this results in a small sapphire pedestal below the nitride pillar. The micropillars are compressed at room temperature in displacement control with a strain rate of $1 \times 10^{-3}\text{ s}^{-1}$. The height of the nitride pillars corresponds to the thickness of the films. In order to account for different mechanical properties of the sapphire substrate and pillars, Sneddon's corrections [21] are applied during load-displacement data processing in the open-source community curated MicroMechanics Data Analyzer.

Details on theoretical calculations of thermodynamic stability and hardness of the high-entropy alloy nitrides are presented in the [Supplementary Note 2](#).

3. Theoretical calculations and discussion

In our calculations, the most likely decomposition products of the high-entropy nitride system are assumed to be unary phases,

and binary and ternary compounds. The crystal structures of the reported phases can be readily accessed in, e.g., ICSD [22]; hence, for the $(\text{TiZrHfVNb})_{1-x}\text{Al}_x\text{N}$ alloys we can calculate the total enthalpies at the same level of accuracy as for the special quasirandom structure (SQS) supercells. The calculated dependence of the formation enthalpies of the $(\text{TiZrHfVNb})_{1-x}\text{Al}_x\text{N}$ alloys increases with the Al fraction, x , and is illustrated in Table 1. High positive values of the formation enthalpies for all x values indicate the instability of the compounds, resulting in decomposition of the phases to ternary and binary compounds. The stabilization temperature is considerably higher than the typical deposition temperature of most PVD methods. Therefore, all alloys within the studied compositional range can be regarded as metastable to less complex solid solution and phases. Moreover, the thermodynamic driving force for decomposition into less complex solid solutions, i.e. ternary compounds, is increasing as a function of x in the solid solution evidenced as the increment of the formation enthalpy difference ΔE . The estimation of Vickers hardness, H_v , for various x values, including the concentrations observed in the experiment (see Supplementary Fig. S3), shows that the Vickers hardness increases as x increases in the solid solution. Importantly, Vickers hardness of Al-free and low- x films with composition observed in the experiment is higher than that of the systems with ideal equimolar composition. The hardness approach relatively similar values at $x = 0.5$.

The electron charge distribution in NaCl $(\text{TiZrHfVNb})_{1-x}\text{Al}_x\text{N}$ alloys is also calculated to study the interatomic bonding via the charge transfer. Bader charge analysis [23] (Table 1 and Supplementary Table 2) is performed and demonstrates an increase of the average interatomic charge transfer with the increase of Al content in the systems, peaking at $x = 0.6$, and then rapid decrease for higher values of x . This trend suggests that alloying with Al continuously changes the interatomic bonding in the solution from covalent to stronger ionic. For a stronger ionic bond, more charges are transferred between the adjacent atoms with shorter bonds as smaller Al atoms substituting TM in the cation sublattice decrease the lattice size. Since Al preferential hybridization is sp^3 , its incorporation into TM-rich cation sublattice destabilizes the *fcc* structure with preferential sp^2d^3 hybridization. This matches the trend of increasing formation energy, both suggesting higher driving force for decomposition of these alloys as a function of Al content.

4. Experimental results and discussion

4.1. Elemental composition

Elemental analysis performed by means of ToF-ERDA and XPS reveals that the nitrogen content is relatively stable among the series of the as-deposited HEN films at 48.05 ± 0.45 at% implying only

a slight substoichiometry with respect to nitrogen (Table 2). The films contain a relatively low concentration of Ar, O, and C impurities with the total concentration of 2 ± 0.2 at%. In particular, O content is in the range of ~ 1 at% implying dense microstructure without porosity [24]. Moreover, the concentration of Ar in the films is ≤ 0.4 at% due to suppressed Ar^+ ion bombardment during film growth, as previously reported for the hybrid growth mode with metal-ion-synchronized bias [16]. The concentration of TMs is relatively equiatomic with a slight variation of about ± 2 at%. This variation can be assigned to the target surface poisoning that changes the sputtering yield of transition metals due to the difference in the enthalpy of nitride formation among the target metals (see Supplementary Table 3). Nevertheless, as the variation is small it is assumed to not qualitatively affect our discussion and conclusions. The fraction of Al in the films $(\text{TiVZrNbHf})_{0.49}\text{Al}_{0.51}\text{N}$ and $(\text{TiVZrNbHfTa})_{0.55}\text{Al}_{0.45}\text{N}$ is slightly different despite the same deposition parameters used for the deposition. This is a consequence of a slightly higher sputtering yield of the alloy target composed of six TMs evidenced as a higher deposition rate of the corresponding films (Supplementary Table 1).

The composition data obtained by XPS and ToF-ERDA are in a good agreement with EDS (Supplementary Table 4). It is apparent from the composition of the films that calculated values of configuration entropy (S_{conf}) are $\geq 1.5R$ per formula unit at the metal sub-lattice for the films with $x \leq 0.51$ (Table 2). Therefore, except for the films with $x \sim 0.6$, all multicomponent nitrides can be classified as high-entropy nitrides even though the composition is not equimolar.

4.2. Microstructure and phase composition

SEM investigations of fracture cross-sections (Fig. 1) reveal a dense microstructure with no open column boundaries in all films. The microstructure of the films without Al and with the lowest Al content features fine fibrous growth morphology without well-visible columnar grains or grain boundaries. With increasing Al content, the columnar growth becomes more clear.

The θ - 2θ XRD patterns for all samples contain exclusively the characteristic (1 1 1), (0 0 2), (3 1 1), and (2 2 2) diffraction peaks typical for face-centred cubic (*fcc*) NaCl-type crystal structure (space group *Fm-3m*) of transition metal nitrides, Fig. 2a, b. This indicates single-phase *fcc* NaCl-structured solid solution formation. A more accurate phase analysis is carried out by measuring θ - 2θ patterns as a function of the sample tilt angle ψ (the angle between the scattering plane defined by the incoming and outgoing X-ray beams and the sample normal), see Supplementary Fig. S4. The results are in good agreement with the complete θ - 2θ patterns in the symmetric configuration. However, broad diffraction reflections with weak intensity on the diffraction pattern of $(\text{TiVZrNbHf})_{0.36}\text{Al}_{0.64}\text{N}$

Table 1

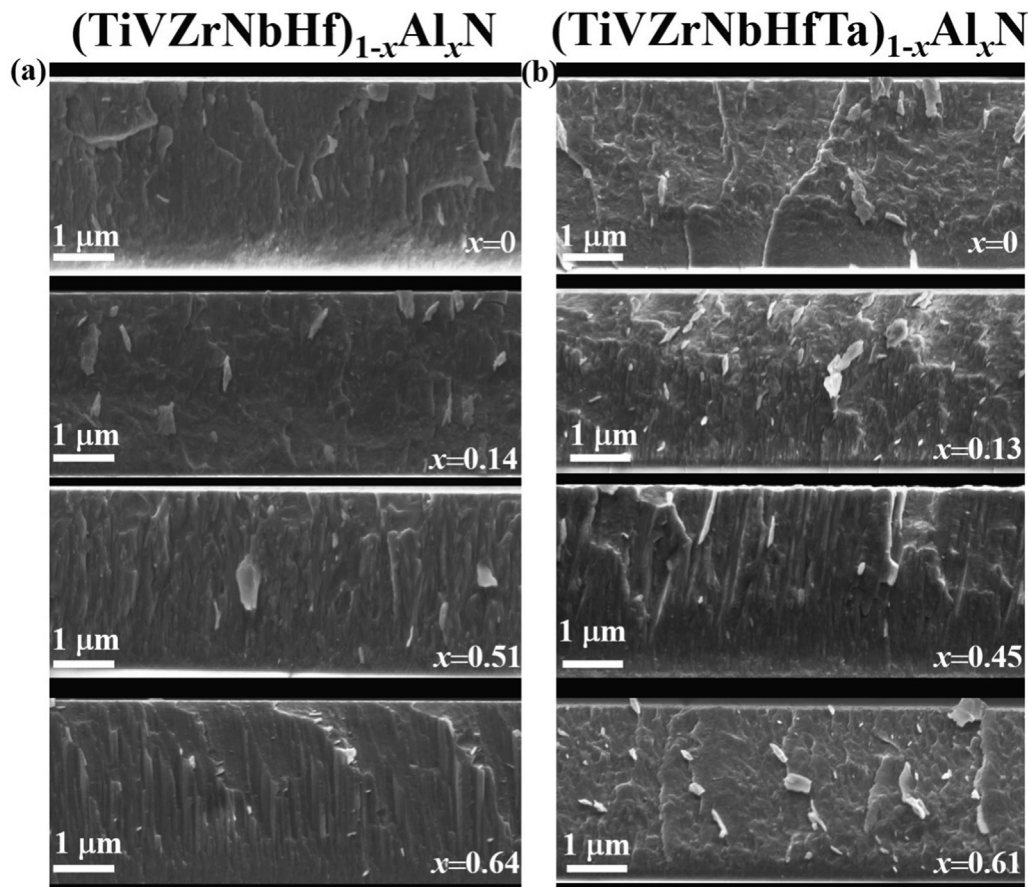
Calculated formation energy, formation energy difference (decomposition into binaries vs. ternaries), stability temperature, electron charge transfer and Vickers hardness of $(\text{TiZrHfVNb})_{1-x}\text{Al}_x\text{N}$ alloys.

x , Al fraction	Formation energy (decompose to binaries) meV/atom	Formation energy (decompose to ternaries) meV/atom	ΔE (ternaries to binaries decomposition) meV/atom	Stability T, C	Average transfer e /atom	H_v , GPa
0	622.5	249.6	372.9	4722.2	0.87	16.74
0.1	454.9	79.24	357.7	3068.3	0.89	17.12
0.2	529.5	151.1	378.4	3598.5	0.89	17.50
0.3	543.1	162.0	381.1	3762.1	0.89	17.89
0.4	558.9	175.1	383.8	4525.9	0.94	18.29
0.5	532.4	121.0	411.4	3467.9	0.97	18.70
0.6	520.3	136.5	465.5	3719.3	1.00	19.12
0.7	501.6	0	501.6	4421.6	0.99	19.54
0.8	558.0	0	558.1	5590.9	0.73	19.98

Table 2

Elemental composition of the samples derived from the combined measurements by means of XPS and ToF-ERDA.

Sample	Composition (at.%)											x, Al fraction	N/Me ratio	S _{conf}
	N	Al	Ti	Hf	V	Zr	Nb	Ta	Ar	O	C			
(TiVZrNbHf)N	48.2	0	11.8	7.6	10.5	12.2	7.8	–	0.4	0.8	0.7	–	0.97	–1.59R
(TiVZrNbHf) _{0.86} Al _{0.14} N	48	6.9	10.3	6.5	9	10.2	6.8	–	0.4	1.0	0.8	0.14	0.97	–1.77R
(TiVZrNbHf) _{0.49} Al _{0.51} N	48.8	25	11.8	7.6	5.1	5.8	3.5	–	0.4	1.0	0.7	0.51	0.99	–1.46R
(TiVZrNbHf) _{0.36} Al _{0.64} N	48.4	31.9	4.1	2.6	4.1	4.1	2.7	–	0.4	1.0	0.7	0.64	0.98	–1.22R
(TiVZrNbHfTa)N	48.2	0	11.5	7.6	6.9	10.4	6.5	6.7	0.5	0.9	0.8	–	0.97	–1.76R
(TiVZrNbHfTa) _{0.87} Al _{0.13} N	47.9	6.7	9.7	6.6	6.5	8.9	5.7	5.7	0.4	0.9	0.9	0.13	0.96	–1.93R
(TiVZrNbHfTa) _{0.55} Al _{0.45} N	47.5	22.6	6.4	4.3	4.3	5.7	3.4	3.5	0.3	1.0	0.9	0.45	0.95	–1.66R
(TiVZrNbHfTa) _{0.39} Al _{0.61} N	47.4	30.1	4.8	3.1	2.9	4.6	2.3	2.4	0.4	1.1	1	0.61	0.94	–1.37R

**Fig. 1.** SEM fracture cross-section images of the (TiVZrNbHf)_{1-x}Al_xN ($x = 0, 0.14, 0.51, 0.64$) (a) and (TiVZrNbHfTa)_{1-x}Al_xN ($x = 0, 0.13, 0.45, 0.61$) (b) thin films on Al₂O₃(0001) substrate.

and (TiVZrNbHfTa)_{0.39}Al_{0.61}N films are found in the range of $2\theta \sim 48$ – 50° and $\psi \sim 39.2$ – 56.8° . These peak positions correspond to (1 0 1 2) Bragg reflection of hexagonal (*hex*) AlN (space group *P63mc*, ZnS-wurtzite prototype) shifted towards lower diffraction angles relative to diffraction lines of pure *hex*-AlN powder. This implies that the lattice of the *hex* phase is expanded due to the incorporation of larger TM atoms into metal lattice sites. The larger full width half maximum of the (1 1 1) reflections, Γ_{111} , of the films with $x = 0.64/0.61$ (Fig. 2d) additionally indicates the formation of a second phase which interrupts the growth of *fcc* phase resulting in the smaller coherently diffracting domain size of the *fcc* phase, i.e. larger Γ_{111} values. It is worth noting that further increase of Al content up to $x \sim 0.7$ causes a more evident formation of *hex* AlN phase in addition to the *fcc* phase (see Supplementary Figure S5). Hence, the maximum solid solubility limit of Al in the *fcc* NaCl-structured high-entropy transition metal nitrides is in the

range $x \sim 0.51$ – 0.64 in (TiVZrNbHf)N and $x \sim 0.45$ – 0.61 in (TiVZrNbHfTa)N. The formation of single-phase solid-solutions with such high Al content with respect to Al solubility limits is a remarkable result, given that 5–7 nitride forming metals are present. Since the purpose of this paper is to explore the single-phase solid-solution nitrides, solubility limit of Al in HENs and impact of *hex*-AlN on the mechanical properties of HENs, the films with Al content higher than $x \sim 0.64$ are excluded in the further analysis.

All diffraction peaks gradually shift toward higher diffraction angles upon Al incorporation (Fig. 2a, b), indicative of a lattice shrinking due to the substitution of transition metal atoms by smaller Al atoms. The composition-dependent lattice parameters are calculated from the (1 1 1) peak positions at $\psi \sim 0$, a_{XRD} , and presented in Fig. 2c. The experimental lattice parameter is compared with linearly interpolated lattice parameters calculated

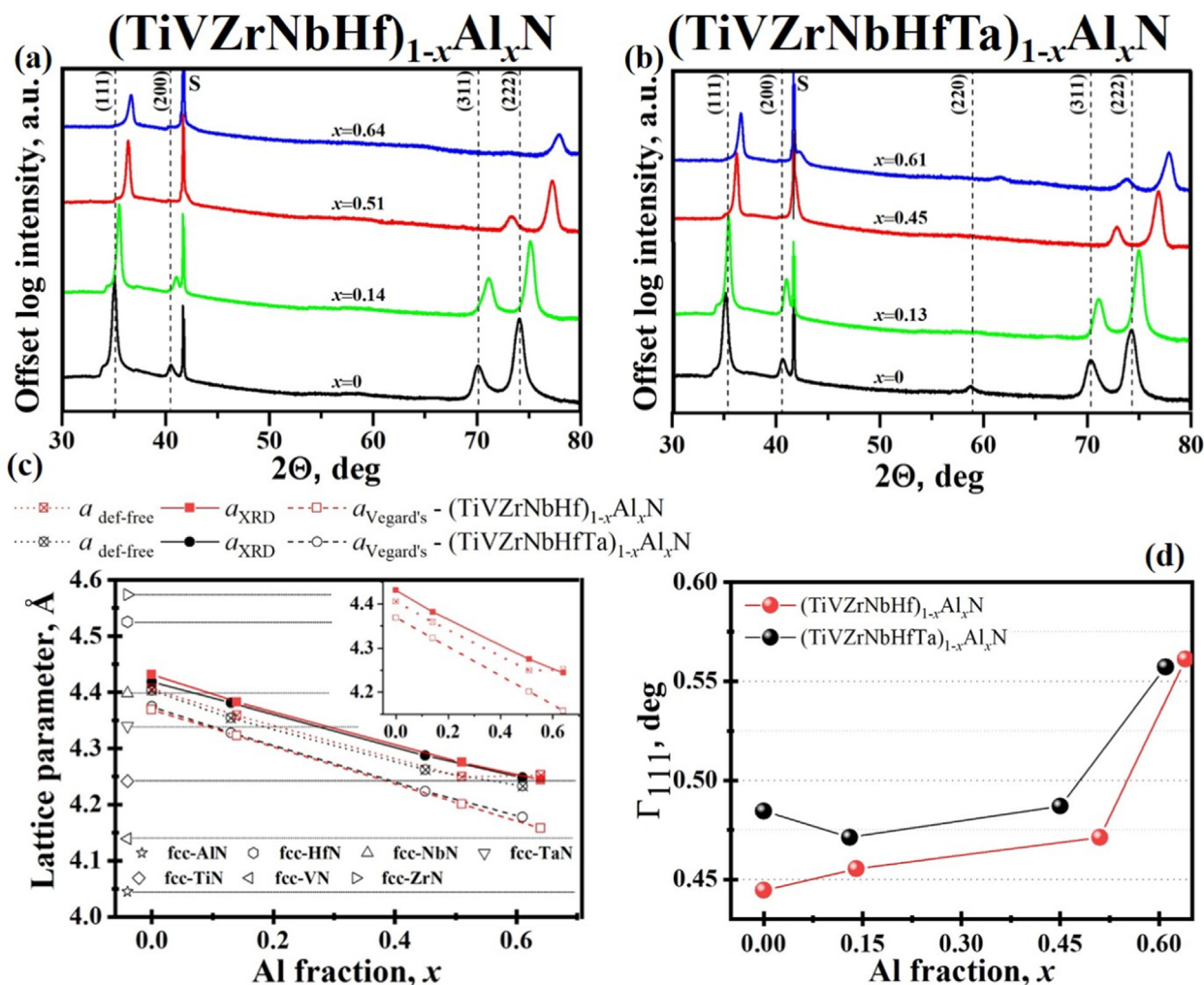


Fig. 2. Offset θ - 2θ XRD patterns for $(\text{TiVZrNbHf})_{1-x}\text{Al}_x\text{N}$ ($x = 0, 0.14, 0.51, 0.64$) (a) and $(\text{TiVZrNbHfTa})_{1-x}\text{Al}_x\text{N}$ ($x = 0, 0.13, 0.45, 0.61$) (b) thin films on $\text{Al}_2\text{O}_3(0001)$ substrate. Black dashed lines correspond to the peak positions of Al free films. Structural analysis data of $(\text{TiVZrNbHf})_{1-x}\text{Al}_x\text{N}$ and $(\text{TiVZrNbHfTa})_{1-x}\text{Al}_x\text{N}$ thin films: evolution of experimental a_{111} and Vegard's lattice parameter (c, the inset shows the a_{111} of the $(\text{TiVZrNbHf})_{1-x}\text{Al}_x\text{N}$ system) and full-width at a half maximum of (1 1 1) XRD peak as a function of x (d).

according to Vegard's empirical rules, $a_{\text{Vegard's}}$, considering the mole fractions of constituent nitrides derived from the XPS/ToF-ERDA elemental analysis and corresponding bulk lattice parameters of binary nitrides (Supplementary Table 3). It is evident that the experimental out-of-plane lattice parameter follows approximately the Vegard's law (Fig. 2c). However, for both systems a clear systematic positive deviation of the experimental a_{XRD} values from this empirical rule is observed. Additional contribution to the increment of the lattice spacing can be caused by residual compressive stresses, as discussed in more detail below. The lattice parameters of (111) and (200) oriented crystallites are determined from θ - 2θ patterns at a set of different tilt angles ψ (Supplementary Fig. S4). The evolution of the a_{111} and a_{200} values as a function of $\sin^2 \psi$ for all alloy composition is shown in the Supplementary Fig. S6. The negative slope of $\sin^2 \psi$ lines implies that all films are in a compressive stress state. The difference in slope for all single-phase films is quite small implying similar stress level. There is a clear shift of $\sin^2 \psi$ lines towards lower a values with increasing Al content that agrees with the evolution of the lattice parameter with x . The shift is constant with ψ angle for the films with low Al content relative to Al-free films, but the shift becomes more oscillating for Al-rich films. This indicates different elastic strain states in the films depending on Al content. The evolution

of a with $\sin^2 \psi$ for the films with the highest Al content deviates from linearity thus attesting to the existence of stress gradients along the thickness of the films or/and local short range ordering effects (ordering vs. clustering). This deviation is the highest in the films with small fraction of hexagonal phase.

A complete stress-strain state analysis is performed in order to extract the stress- and defect-free lattice parameter, a_{def} , of the HEN thin films. The residual stress obtained from substrate curvature measurements is compressive in all films (see Supplementary Table 5). The compressive stresses in thin films deposited under ion bombardment are generated through the atomic peening mechanism when energetic ions bombarding the growing film induce shallow collision cascades that result in incorporation of extra atoms into the growing film (self-interstitial, vacancies and antisite defects). Considering triaxial hydrostatic stresses in the films (see Supplementary Note 3), it can be deduced that the compressive stresses in the present films are caused preliminary by TM_N antisite defects with lower impact of interstitial defect that is in agreement with previous analysis of the origin of compressive stresses in TiN thin films using triaxial stresses model [25]. Although antisite defects are less thermodynamically preferred in NaCl lattice than vacancies and interstitials, as is predicted by ab initio calculations [26], the formation of antisite defects is

expected under non-equilibrium (quenched) growth conditions and intense ion irradiation during growth of the films. The defect formation in the films deposited in DC mode and hybrid DC/HiPIMS mode is in the first instance determined by types of ions bombarding the growing films: primary Ar^+ in DC mode and Al^+ in DC/HiPIMS mode. The fraction of ionized flux is different in DC and HiPIMS/DC modes that implies different effects on defect generation with Ar^+ or Al^+ ions. Another possible reason for stress generation is the cross-contamination of Al and alloy targets that can cause formation of TM ions (due to relatively low second ionization potential of Ti and V [27]) and subsequent severe recoil implantation (due to higher TM ion mass than that of Al). Although Γ_{111} depends on defect density (area, line and point defects), lattice distortion and the size of coherently diffracting domains, a slightly larger Γ_{111} of the Ta-containing films (Fig. 2d) can be assigned to higher defect density in these films due to more intense TM ion bombardment of the growing film and/or smaller domain size. The formation of *hex*-AlN phase causes relaxation of compressive stresses in Al-rich dual-phase films evident as decrease of the slope of $\sin^2 \psi$ lines.

The triaxial stress model allows to calculate a true “stress- and defect-free” lattice parameter (see Supplementary Note 3) of the HEN thin films (Fig. 2c). The stress- and defect-free lattice parameter is still positively deviate from Vegard’s linear interpolation, but the deviation is lower compared to the deviation of d_{XRD} . The observed positive deviation can be assigned to the fact that simple hard sphere model used for calculation of Vegard’s lattice parameter is not sufficient for evaluating the lattice parameter of high-entropy alloys. The recent studies show that the atomic radii of the metal atoms in the multicomponent surroundings of HEAs deviate from its average size assumed by hard sphere model due to local chemical interactions, i.e. charge transfer effects [28].

Further structural analysis of the films is performed by means of TEM and EDS. Considering that HEN films demonstrate very similar structural and compositional features, TEM is performed only for $(\text{TiVZrNbHf})_{1-x}\text{Al}_x\text{N}$ layers ($x = 0, 0.51, 0.64$). Bright field (BF) and dark field (DF) TEM images of the films shown in Fig. 3 reveal a dense microstructure with no open boundaries or porosity. The films exhibit epitaxial growth of 111-oriented domains well-visible as a thin layer near the interface with the substrate with a uniform contrast on BF and DF images and symmetric NaCl reflections on the SAED acquired from the substrate/film interface along the $[1\bar{1}00]$ zone axis of the substrate and $[1\bar{1}0]$ zone axis of the films (Fig. 3d, j, r). The reflections are aligned symmetrically to the reflections of Al_2O_3 implying local epitaxial growth. The epitaxial growth takes place with at least two different in-plane orientations of $\langle 111 \rangle$ domains evident as two sets of $[1\bar{1}0]$ zone axis reflections slightly misaligned in relation to each other implying the formation of twin boundaries (yellow/red circles and squares in Fig. 3d). The 111-oriented epitaxial growth of TMNs on $\text{Al}_2\text{O}_3(0001)$ is a typically well-known phenomenon due to a relatively low mismatch between their lattices when $[21\bar{1}0]$ direction of $\text{Al}_2\text{O}_3(0001)$ coincides with $[101]$ direction of TMNs $(1\bar{1}1)$ [29]. At the same time, the epitaxial growth of HENs is rarely reported and remains poorly studied [30]. The epitaxial growth proceeds up to 100 nm of the film thickness when renucleation sets in. The onset of the mixed polycrystalline growth is clear on the SAED of Al-rich films (Fig. 3j and r) as a slight angular elongation of the reflections. The epitaxial growth gradually changes to random nucleation of small grains and further development of fine-fibrous microstructure with mixed polycrystalline orientations. During early growth stage the films exhibit fine-fibrous columnar microstructure with column diameters of $\sim 20\text{--}30$ nm that continuously evolve from the nucleation layer towards the surface where larger grains (80–100 nm) near the film surface are observed (insets in Fig. 3 a, b, h, k, o, s). SAED of the Al-free single-phase films

(Fig. 3c) clearly show no preferential orientation, but numerous randomly oriented crystals evident as rings with non-uniform angular intensity of $(1\bar{1}1)$ and (002) reflections of *fcc* NaCl structured phase that is in agreement with XRD (Fig. 3c). At the same time, $(\text{TiVZrNbHf})_{0.49}\text{Al}_{0.51}\text{N}$ thin films are composed of slightly larger columnar grains (with the same aperture size, SAED contains intense spots with low angular dispersion, Fig. 3i) extending from the nucleation layer towards the surface and with a slight dominance of (001) grains (see Supplementary Fig. S7). This dominance of (001) grains can be attributed to the lower Al diffusion activation barrier on TMN $(1\bar{1}1)$ surface than that of TM adatoms (reasoning extrapolated to all TMN from the first principle calculations performed for TiAlN system [31]). Low-resolution cross-sectional HAADF-STEM images of the $(\text{TiVZrNbHf})\text{N}$ and $(\text{TiVZrNbHf})_{0.49}\text{Al}_{0.51}\text{N}$ films (Fig. 3e and Fig. 3l) show that the films are homogeneous at the microscale in all directions in agreement with STEM-EDS cross-sectional mapping (Fig. 3f, g and Fig. 3m, n, respectively).

Al-rich $(\text{TiVZrNbHf})_{0.36}\text{Al}_{0.61}\text{N}$ thin films show clear diffraction spots associated with *hex*-AlN phase (Fig. 3p and Supplementary Fig. S7). A pronounced segregation of Al-rich (dark contrast) and TM-rich (bright contrast) phases in lateral dimension is observed in Z-contrast HAADF-STEM images of the $(\text{TiVZrNbHf})_{0.36}\text{Al}_{0.61}\text{N}$ thin films (Fig. 3t) that additionally confirms the formation of Al-rich hexagonal phase. The hexagonal phase segregates along TM-rich column boundaries of *fcc* phase and exhibit continuous local epitaxy with columns extending throughout the film. Moreover, the lattice of the hexagonal phase is expanded relative to the pure *hex*-AlN (cf., Supplementary Fig. S7), thereby additionally confirming incorporation of TMs into the *hex*-AlN lattice. Preservation of the columnar structure in the film with $x = 0.61, 0.64$ can be assigned to the absence of renucleation during growth due to small size and low density of these AlN-rich precipitates and continuous Al^+ bombardment of the growing film that supplies Al to both *fcc* and *hex* phases. Both *fcc* and *hex* phases contain TMs as evident from EDS mapping (see Supplementary Fig. S8), SAED, XRD, and XPS (see below).

Fig. 4 shows selected areas of the cross-sectional high-resolution STEM (HRSTEM) images of the films with corresponding FFT and FFT-filtered images. HRSTEM images of the grains of the films show clear uniform contrast attesting to a homogeneous phase without segregations or ordering in the single-phase films. The FFT-filtered images (Fig. 4b, i, o) are generated using the FFT reflections marked by red circles in Fig. 4c, j, p. These allow to reveal misfit dislocations (positions marked with rectangles in Fig. 4b, i, o) and stacking faults, SFs, (positions marked with ovals in Fig. 4b, i, o) in all films, which are resolved in the enlarged FFT-filtered images (Fig. 4e, f, l, m, r, s).

Fig. 5a, b shows Raman spectra of the $(\text{TiVZrNbHf})_{1-x}\text{Al}_x\text{N}$ ($x = 0, 0.14, 0.51, 0.61$) (a) and $(\text{TiVZrNbHfTa})_{1-x}\text{Al}_x\text{N}$ ($x = 0, 0.13, 0.45, 0.64$) thin films. The Raman spectra of HEN thin films displays first order transvers and longitudinal acoustic peaks in acoustic frequency range and first order optical modes in optical frequency range. The scattering in acoustic range is associated with vibrations of heavy metal atoms and vibrations of the lighter N atoms correspond to the scattering in the optical range. Raman scattering in transition metal nitrides occurs due to any deviation from stoichiometry and associated formation of vacancies or antisite defects [32]. However, we speculate that Raman scattering in HENs is preferentially determined by lattice symmetry breaking due to severely distorted cation sublattice caused by atomic size mismatch of metallic elements. Apparently, with increase of Al content in the cation sublattice the symmetry breaking associated with lattice distortion (δ), Fig. 5c, increases giving rise to more Raman active vibrations. Although the anion sublattice is not distorted due to one sort of atom on the anion sites, the cation and anion

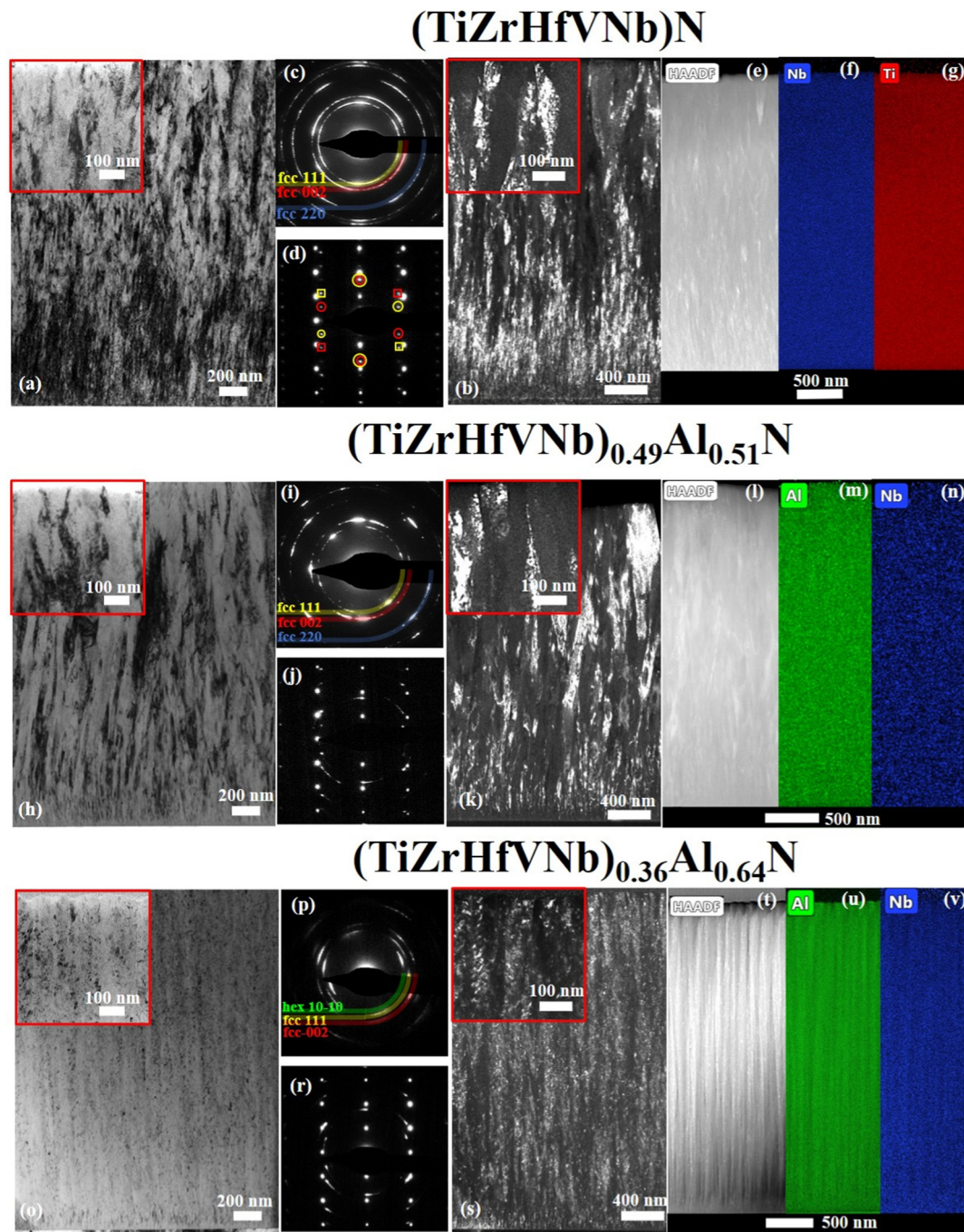


Fig. 3. Typical cross-sectional TEM images, SAED patterns, HAADF images, and EDX mapping, from $(\text{TiZrNbHf})_{1-x}\text{Al}_x\text{N}$ thin films ($x = 0$ (a-g), $x = 0.51$ (h-n), $x = 0.64$ (o-v)). The insets in (a, b, h, k, o, s) show a magnified BF/DF images of a near surface area of corresponding films.

sublattices of TMN are chemically dependent as determined by octahedrally coordinated TM atoms by the nitrogen ligands forming sp^3d^2 hybridization with e_g and t_{2g} symmetry along $\langle 100 \rangle$ and $\langle 110 \rangle$ directions of cubic crystal, respectively [33]. Therefore, the sublattices give dependent Raman contribution as evidenced by synchronous increase of intensity of all bands with increase of Al content in the films. Consequently, the increase of intensity of first order O mode attests for the change in lattice ordering around N atoms.

It is worth noting that the penetration depth, reflectivity and absorption of light can change as a function of x , thus impacting the Raman intensity, but this change can be considered to be

negligibly small in the optical spectral range [33]. The shift in position of all lines to higher frequencies with increasing Al content can be attributed to a linear decrease of the lattice constant and hence to cation to N bond length. Additionally, the shift of acoustic lines to higher frequencies can be related to a decrease of VEC per unit cell (Fig. 5d) leading to phonon softening as concentration of Al increases in the solution [34]. Although the Raman peak shift can be also caused by piezo-spectroscopic effect occurring as a result of straining of interatomic distance in response to compressive residual stresses, its magnitude relatively less meaningful being in the range of $\pm 2.5 \text{ cm}^{-1} \text{ GPa}^{-1}$ typical for TMNs [35]. The intensity of Raman bands of the hexanary dual-phase film is similar to

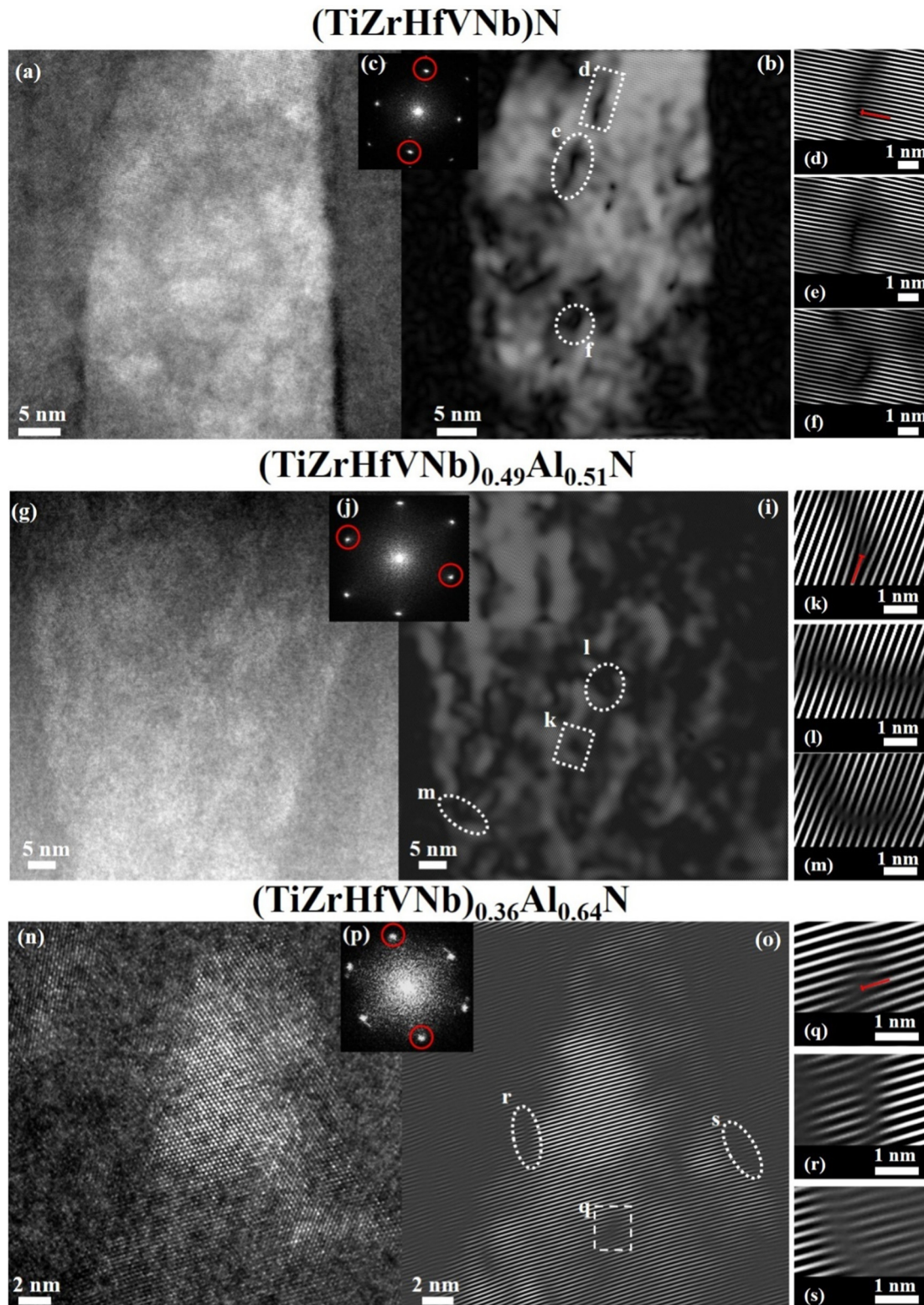


Fig. 4. Cross-sectional HRSTEM images of $(\text{TiZrNbHf})_{1-x}\text{Al}_x\text{N}$ ($x = 0$ (a), $x = 0.51$ (g), $x = 0.64$ (n)) thin films, corresponding FFT images (c, j, p), FFT filtered images generated using the reflections marked by red circles (b, i, o), and enlarged FFT filtered images taken from the positions marked with rectangles and ovals showing misfit dislocations (d, k, q) and stacking faults (e, f, l, m, q, r, s), respectively.

the intensity of the peaks from the hexanary single-phase film with $x = 0.51$, whereas the intensity of Raman bands of the heptanary dual-phase film is higher than the intensity of the peaks from the

heptanary single-phase film with $x = 0.45$. This can be associated with higher Al content in the fcc lattice of the heptanary dual-phase film and, thus, larger lattice distortion.

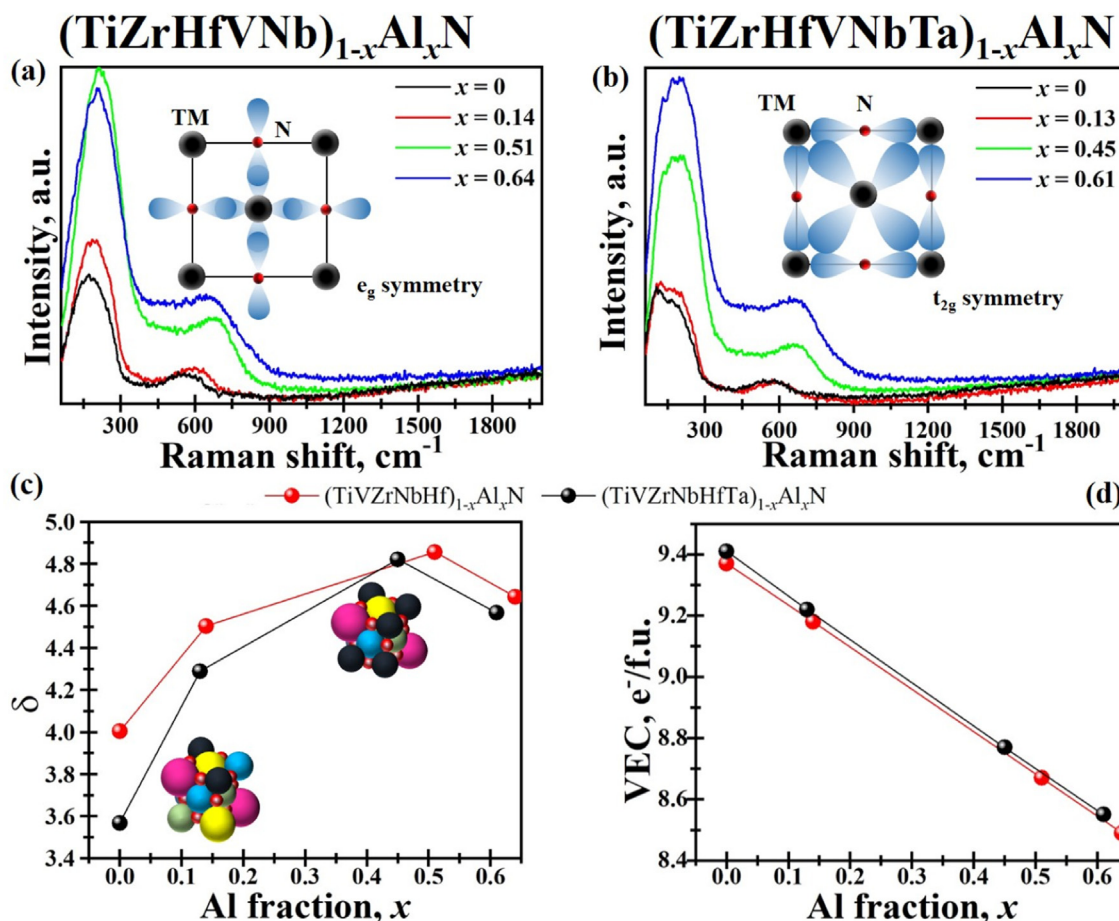


Fig. 5. Raman spectra of the $(\text{TiVZrNbHf})_{1-x}\text{Al}_x\text{N}$ ($x = 0, 0.14, 0.51, 0.64$) (a) and $(\text{TiVZrNbHfTa})_{1-x}\text{Al}_x\text{N}$ ($x = 0, 0.13, 0.45, 0.61$) thin films and corresponding calculated lattice distortion (δ) (c), and VEC $e/f.u.$ (d).

4.3. Chemical bonding

The core-level signals from the hexanary HEN thin films with different Al content are compared in Fig. 6 (a)–(e) that show the main metal core levels spectra of Ti 2p, V 2p, Zr 3d, Nb 3d, and Hf 4f. Fig. 7 (a) and (b) demonstrate N1s and Al2p spectra. Due to space restrictions the core-level spectra of the heptanary HEN thin films are presented in the Supplementary Fig. S9 and S10. The satisfactory fit of the core-level spectra with correctly constrained peak ratio for all spin-split doublets allows to resolve the contributions corresponding to metal-nitrogen bonding, N-deficient TM-N bonding, and satellite peaks (at a higher binding energy (BE) side with respect to the primary metal peaks). The presence of peaks due to N-deficient TM-N bonding is attributed to an artefact of Ar^+ ion etch which causes the substoichiometric nitride layer formation due to preferential resputtering of lighter N atoms, in agreement with previous studies of corresponding binary nitrides [34]. The BE values for N 1s, Al 2p, and TM main core level peaks of the HEN thin films are listed in Supplementary Table 6 and compared with ISO-calibrated binding energy values of the corresponding binary nitrides measured using the same instrument. In majority of cases, the main TM core-level peaks shift towards higher BE side and Nb 3d and Ta 4f peaks shift towards lower BE side with increasing Al content in the films up to $x \sim 0.51/0.45$ (see Supplementary Table 6). At the same time the corresponding N 1s peaks shift towards lower BE side. To present a reliable interpretation of core-level shifts in terms of charge transfer, not affected by reference level effects [19], the relative

BE difference between main metal peaks and the N1s peaks is plotted in Fig. 7c as a function of x . When considering that BE is preliminary determined by the initial state contribution of the valence charge density on an atom, the increase of the Ti 2p-N1s and V 2p-N 1s difference (Ti 2p and V 2p are at higher BE than N 1s) and the decrease of the Hf 4f-N 1s, Zr 3d-N 1s, Nb 3d-N 1s, and Ta 4f-N 1s difference (Hf 4f, Zr 3d, Nb 3d, and Ta 4f are at lower BE than N 1s) with x unambiguously points on the charge transfer from TM to nitrogen as Al content increases in the solid solution implying that the bonding character in HENs changes from covalent/metallic in Al-free films to more ionic in Al-rich single-phase films. The charge transfer from TM to N atoms is confirmed by ab initio calculation of Bader charge transfer (Table 1 and Supplementary Table 2), which supports our interpretation of XPS results. Although the Ta and Nb core-level peaks shift to lower BE, the magnitude of N 1s shift towards lower BE is higher that results in the increment of the BE difference. Moreover, it is apparent that the BE of core level electrons in TM atoms in Al-free solid solution is lower than that in corresponding binary nitrides (Supplementary Table 6), that indicates that the valence charge density on metal sites is higher in the former case. Al-free solid solutions have relatively high valence charge density on TM sites due to filled d-type orbitals (see Supplementary Table 3) which is typical for NaCl-structured TMNs sp^3d^2 hybridization. The directional covalent bond e_g of sp^3d^2 hybridization accommodates 6 electrons (two metal s, one metal d and three nitrogen p) and any additional valence electron has to populate orbitals with t_{2g} symmetry or antibonding states. Therefore, the electron density remaining after

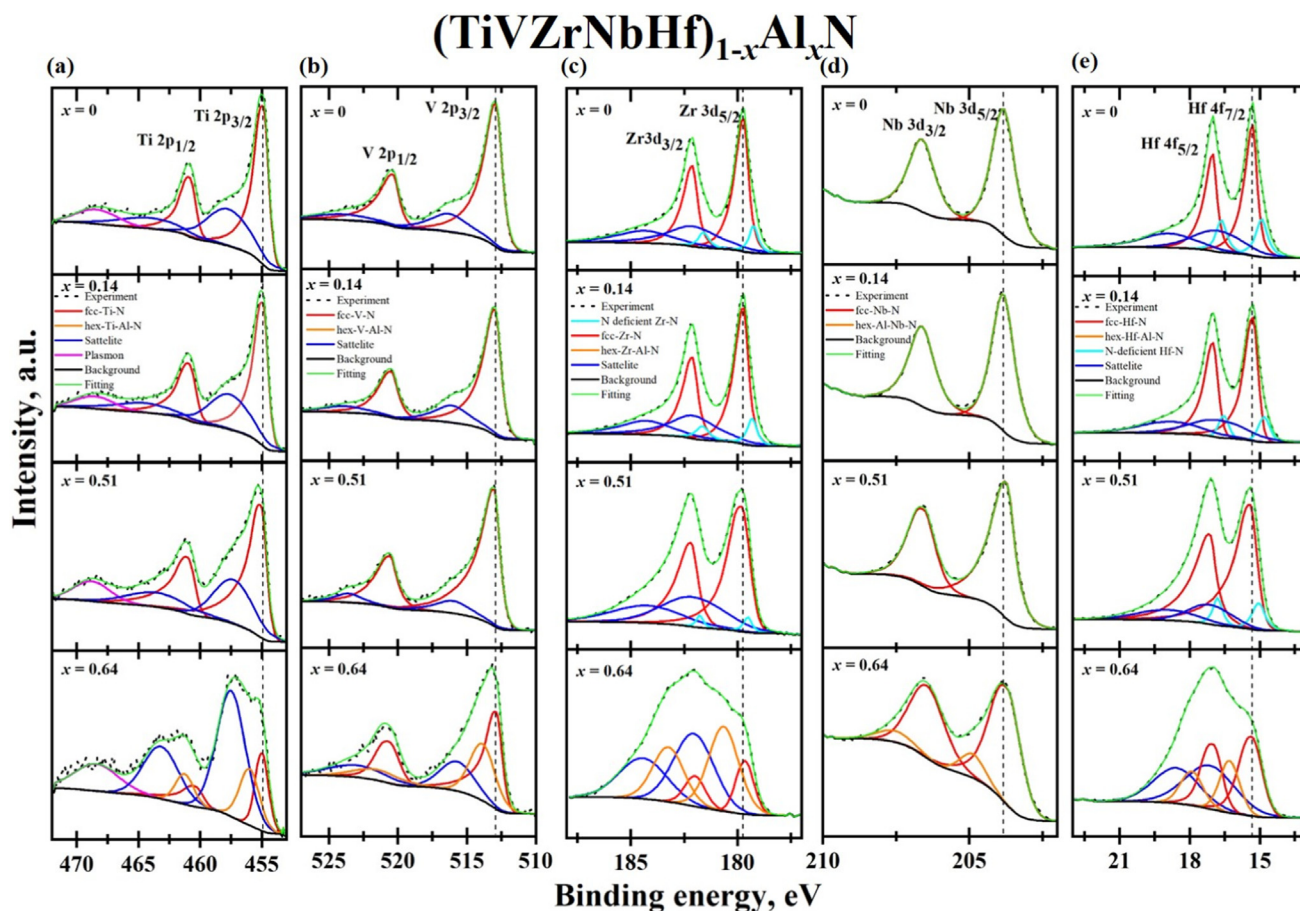


Fig. 6. Ti2p (a), V2p (b), Zr3d (c), Nb3d (d), and Hf4f (e) core-level XPS spectra acquired from $(\text{TiVZrNbHf})_{1-x}\text{Al}_x\text{N}$ thin films ($x = 0, 0.14, 0.51, 0.64$). Black dashed lines correspond to the peak positions of Al-free films.

filling e_g orbitals populate t_{2g} orbitals in Al-free solid solution with $\text{VEC} \sim 9.4 e^-/\text{f.u.}$ that, in turn, leads to the increment of the metallic d-d interaction and more metallic character of the bonding as evident from the XPS valence band spectra as an increase of the volume density of $d-t_{2g}(\text{Me})$ orbitals at BE near 1 eV (Fig. 7d, e). The lower BE of core-level electrons of TM atoms in the HENs than in corresponding binary nitrides can be assigned to so called synergistic “cocktail” effect of different TM atoms in the NaCl structured solid solution. Bader charge analysis shows that there is a charge transfer from Ti, Zr and Hf atoms to V and Nb atoms in Al-free system (see Supplementary Table 2) that is expected since Ti, Zr, and Hf have smaller electronegativity values than V and Nb. However, all TM core-level peaks are shifted towards lower BE in Al-free HENs film compared to binary nitrides (Supplementary Table 6). This can be explained by the fact that local atomic environment in the solid solution of HENs differs from the configuration used for DFT calculations whereas the charge density on TM atom in multicomponent systems is additionally determined by their first and second nearest-neighbours [28]. Moreover, as changes in the BE with lattice strain are dominated by initial state affects [35], reducing interatomic bonding (evident as the decrement of the stress-free lattice parameter) leads to the larger charge density on N atoms that can also contribute to the lower BE of N electrons in Al-rich HEN thin films in addition to the increment of valence charge on the N atoms due to ionic bonding character. Ultimately, substitution of TM atom by Al gradually weakens the sp^3d^2 hybridization due to lower valence electron concentration of Al (see Supplementary Table 3) and promotes the formation of sp^3 hybridization preferential for Al-N bonding in hexagonal structure.

The Al 2p peaks of the low x and Al-rich NaCl solid solutions are fitted with one primary component whose BE is similar. For the Al-rich dual-phase HEN film, the Al 2p peak is fitted with additional component with BE values typical for *hex*-AlN implying the presence of sp^3 rich hybridization and formation of *hex*-AlN phase in the film (consistent with XRD and TEM). Hf 4f, Zr 3d, V2p, Nb3d, and Ti 2p core level spectra of Al-rich dual-phase films ($x > 0.6$) undergo distinct changes: in addition to an increase of the satellite peak intensity, additional spin-orbit doublets appear at higher BE side relative to the main peaks. At the same time, the components of TM core level peaks corresponding to the TM atoms in NaCl lattice remain at the same BEs. Considering that the appearance of these new components is associated with dual-phase composition in corresponding films as revealed by XRD and TEM, these high BE doublets are assigned to electrons originating from Hf, Zr, V, Nb, and Ti atoms in hexagonal AlN lattice [36].

It worth noting that HEN thin films containing Ta show a very similar trend and additionally Ta 4f core-level spectrum contains high BE peak component associated with Ta atoms incorporated into hexagonal lattice (see Supplementary Figs. S7 and S8).

The analysis of the elemental composition, microstructure, phase composition and chemical bonding of the films provides sufficient evidence to conclude that single phase solid solution $(\text{TiVZrNbHf})_{1-x}\text{Al}_x\text{N}$ and $(\text{TiVZrNbHfTa})_{1-x}\text{Al}_x\text{N}$ decompose into TM-rich *fcc* and Al-rich *hex* solid solutions when Al content in *fcc*-structured solid solutions reaches a solubility limit that lies between $x = 0.51$ – 0.64 and $x = 0.45$ – 0.61 , respectively. The solubility limit of Al in TMNs is determined by both kinetics during film growth and thermodynamics of constituent phases. Most binary

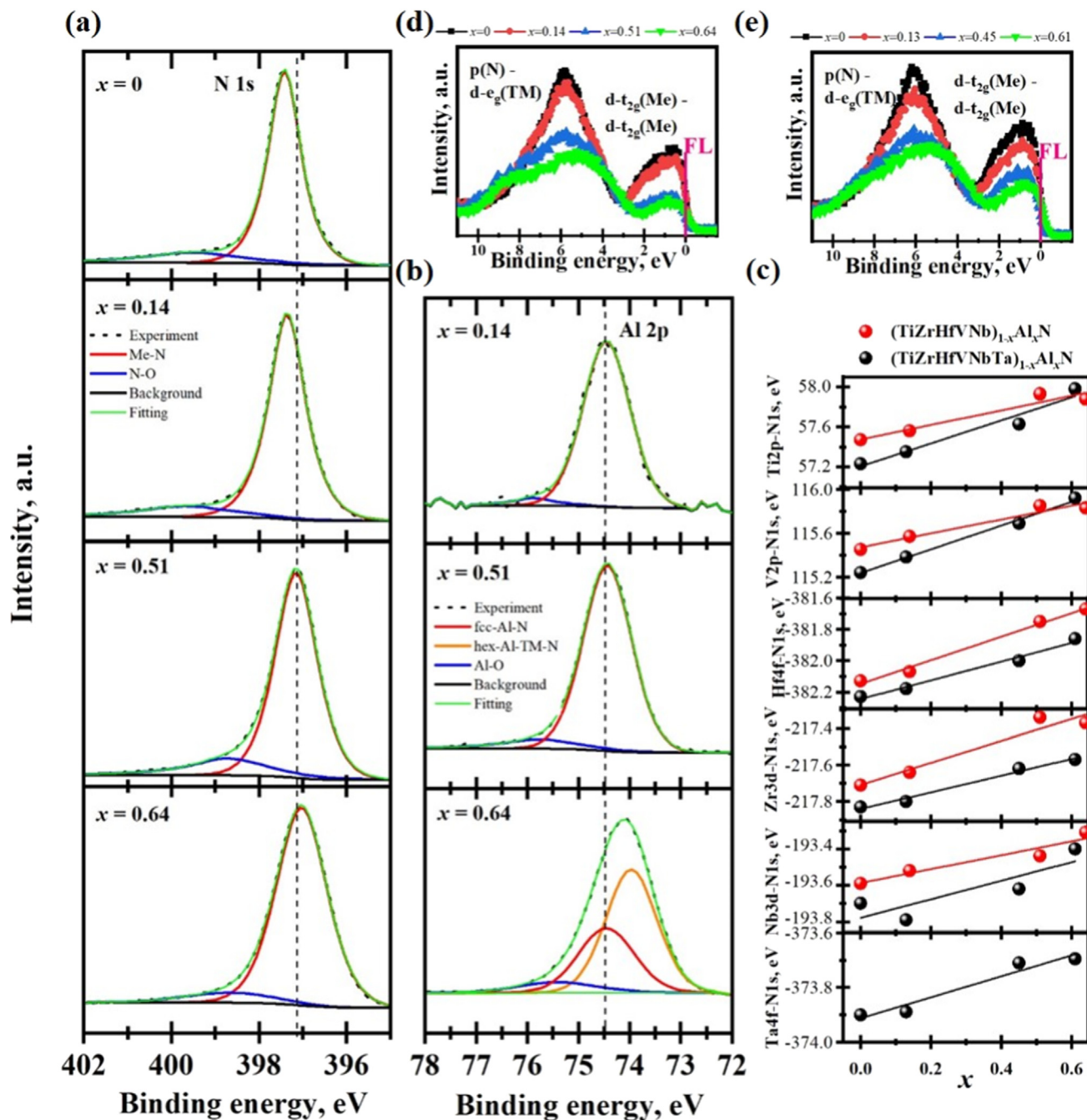


Fig. 7. N 1s (a) and Al 2p (b) core-level XPS spectra acquired from $(\text{TiZrNbHf})_{1-x}\text{Al}_x\text{N}$ thin films ($x = 0, 0.14, 0.51, 0.64$). Black dashed lines correspond to the peak positions of Al free films. (c) Binding energy difference between N 1s-TM in the HEN thin films as a function of Al fraction. XPS valence band spectra from $(\text{TiZrNbHf})_{1-x}\text{Al}_x\text{N}$ ($x = 0, 0.14, 0.51, 0.64$) (d), and $(\text{TiZrNbHfTa})_{1-x}\text{Al}_x\text{N}$ thin films ($x = 0, 0.13, 0.45, 0.61$) (e).

TMNs are soluble in one another due to low cation size mismatch and low/negative enthalpy of formation, such as ZrN-HfN [37], TiN-TaN [38], ZrN-TaN [38], HfN-TaN [38], VN-TiN [39], and TiN-NbN [40]. While there are immiscible pairs such as ZrN-VN [39], TiN-ZrN [41], and TiN-HfN [37]. The miscible pairs of TMNs and presence of immiscible TMN pairs in the multicomponent solid solution of the HENs are opposite forces driving the solid solution to stability or decomposition, respectively. Additional alloying of the system with Al provides even higher driving force towards decomposition because Al is immiscible with all constituent binary nitrides. This is evident as an increase of the formation energy as the concentration of Al on the cation lattice sites increases (Table 1), and is mainly driven by increasing cation size mismatch

and the increasing electronic incompatibility as TMNs favor sp^3d^2 hybridization while Al prefers tetrahedral sp^3 . The ab initio calculations presented above show that all systems are metastable with respect to all corresponding equimolar lower-entropy binary and ternary nitride phases. However, non-equilibrium conditions of PVD provided by high effective temperature of the plasma (10^4 – 10^5 K) and low substrate temperature (rapid quenching on the order of 10^{12} K s^{-1}) kinetically hinder the system to reach the thermodynamically-driven equilibrium and single-phase metastable supersaturated solid solutions form during growth of the films. Additionally, continuous Al^+ subplantation below the high-mobility surface zone during film growth triggers local diffusion on the cation sublattice of NaCl-structured solid solution [12]. This

is achieved by combining high-intensity temporal fluxes of Al⁺ metal ions from Al-HiPIMS superimposed onto the continuous flow of TM neutrals from HEA-DCMS. Under these conditions, TM atoms reside within the high mobility surface layer and upon gas-ion bombardment form TM-rich TMAIN NaCl-structured crystallites, while energetic Al⁺ ions accelerated in the electric field of the substrate are directly implanted into these grains buried below the high-mobility surface. This allows to avoid the formation of thermodynamically favored *hex*-AlN phase and promote the formation of metastable supersaturated NaCl-structured phase. Although there is a strong dependence of the non-equilibrium solubility of Al in TMNs on the growth conditions, a comparison of the solubility limit of Al in HEN and corresponding binary nitrides (synthesised by PVD, see Supplementary Table 3) shows that Al solubility in HENs is higher than that in NbN, HfN, ZrN, TaN, but lower than in VN and TiN. Therefore, the achieved solubility of Al in the HENs can be assigned to “cocktail” effect due to synergetic effect of soluble TMNs, kinetic conditions constraining formation of thermodynamically favoured *hex*-AlN and Al⁺ subplantation boosting the formation of metastable NaCl solid solution during growth of the films. The configuration entropy decreases with increasing AlN content in the films and therefore cannot have an impact on stabilization of the Al-rich solid solution. However, a recent theoretical study demonstrates that severe lattice distortion rather than configuration entropy highly contribute to stabilization of Al-containing multicomponent TM based nitride systems against decomposition [42]. Intriguingly, the Al-rich compositions ($x = 0.51$ in hexanary HENs and $x = 0.45$ in heptanary HENs) have the highest lattice distortion (Fig. 5c) that together with kinetic constraints can compete the electronic incompatibility.

4.4. Mechanical properties

Mechanical properties of the HEN thin films are studied by means of nanoindentation, nanoindentation toughness testing and *in situ* SEM micro-pillar compression. This set of techniques allows to determine a range of mechanisms of deformation taking place in the HEN thin films.

The mechanical properties as a function of Al content are presented in Fig. 8. The indentation hardness of Al-free and low- x films is very similar within the experimental error (Fig. 8a). For hexanary films the hardness increases from about 30.86 ± 1.34 GPa with $x = 0$ to 34.68 ± 2.06 GPa with $x = 0.51$, while for heptanary layers the corresponding values are 29.41 GPa with $x = 0$ and 33.09 ± 1.85 GPa with $x = 0.45$. Further increase of the Al content and transformation to dual-phase structure is accompanied with a decrease of the hardness of the films. The Young's modulus follows the same trend (Fig. 8b). The hardness of TMNs is typically associated with intrinsic effects due to the nature of the chemical bonding and extrinsic effects due to atomic/microstructural features such as solid solution hardening, precipitation hardening, grain boundary hardening and work hardening [43]. Considering that the grain size and microstructure of the films is very similar, the grain boundary hardening can have a relatively similar effect on the measured hardness. The hardness at electronic level is determined by a particular band of σ bonding states between the nearest-neighbor p (N) orbitals and metal d_{eg} orbitals. Full filling of these states at VEC of about 8.4 e⁻/f.u. [44] and low density of shear sensitive metallic d-d bonds (Fig. 7d,e) result in a high density of strong bonding and resistance to shear strain. Additionally, solid solution hardening, as a result of compressive stress field being a consequence of the lattice distortion (reaching maximum at $x = 0.51$ of hexanary HEN and $x = 0.45$ in heptanary HEN, Fig. 5c), can serve as an additional obstacle for dislocation motion. Therefore, the relatively high hardness of the Al-rich single-phase thin films ($x = 0.51/0.45$) can be assigned to two complementary mechanisms. The lower hardness in Al-free and low- x

films can be caused by mechanisms working in opposite directions – high density of shear sensitive metallic d-d interactions (Fig. 7d, e) because of VEC of ~ 9.4 e⁻/f.u. and lower lattice distortion (Fig. 5c). Theoretical calculations show that at VEC around ~ 9.5 e⁻/f.u. a higher occupancy of metallic d-d electronic states induced by the valence electrons of TMs enable formation of metallic bonding promoting a lower shear resistance [10,45]. However, the high VEC in Al-free and low- x systems can promote an additional effect that is based on formation of SFs due to equal energy of a wide range of *fcc*- and *hex*-structured binary TMNs present in the solid solution of HENs [46]. The hardness, thus, can be additionally increased by restriction of dislocation motions across the SFs in materials with VEC ~ 9.4 e⁻/f.u. Since the SFs are present in all films, they can contribute to mechanical properties of the films at the same level. The lowest hardness of dual-phase film is apparently associated with the formation of a softer Al-rich hexagonal phase. At the same time, the increase of hardness and Young's modulus as a function of Al content (up to $x = 0.51/0.45$) can be due to stronger ionicity of the bonding as evident from XPS and Bader charge analysis [47]. The measured experimental and theoretical hardness of the single-phase solid solutions follows the same trend – increasing with the increase of Al fraction (e.g. H_V in Table 1 and H on Fig. 8a). However, the apparent values of hardness derived from experiment and theoretical calculations are different owing to various strengthening mechanisms in polycrystalline experimental samples, which are not accounted for in theoretical calculations.

Nanoindentation toughness measurements are performed using a cube-corner indenter in order to induce deformation of a large volume of the films. The SEM images of the residual imprints after the indentation with lowest applied load of 80 mN and the highest applied load of 500 mN are presented in Fig. 9 with load-displacement curves corresponding to 500 mN load (Supplementary Fig. S11 shows the load-displacement curves corresponding to 80 mN load). No radial cracks at the indenter corner are observed after the indentation of the single-phase thin films at load 80 mN, which corresponds to a penetration depth of less than 30% of the films thickness (Fig. 9 a,b and Supplementary Fig. S11). Even higher indentation load does not cause pronounced cracks in the single-phase films, with exception for $x = 0.51/0.45$ films, in which case lateral cracks and small spallation/delamination zones are present as evident in SEM images and small pop-ins on the corresponding load-displacement curves (Fig. 10 c and d, and insets). A significant pile-ups at the facets of the indenter are formed in the single-phase films, implying plastic flow and, hence, a relatively good ductility. The absence of the radial cracks in most of the single-phase films can be explained by the suppression of the tensile stress field (initiating radial cracks) created by the sharp edge of the indenter, as a result of the high in-plane residual compressive stresses [48]. At the same time, the dual-phase films demonstrate complex residual damage at 500 mN load based on the networks of residual cracks and spallation visible in the SEM image and pop-in events encountered in load-displacement curves.

Although the formation of lateral cracks can be associated with lower toughness of the films, the lateral crack can arise once a sufficient bending of pile-up material occurs. Moreover, there are clear pile-ups in the films with $x = 0.51/0.45$ at 80 mN load but less pile-up material after 500 mN, and therefore the latter can be associated with the delamination of a high fraction of plastically-deformed material. Additionally, the pop-in events in the film with $x = 0.51$ cannot be unequivocally associated to crack initiation in the film, but rather also the internal, sub-surface nonvisible lateral cracks occurred at the film/substrate interface before appearing on the coating surface [49].

The indentation of the dual-phase thin films induces a complex crack network, but the absence of obvious residual damage around the impression in single phase films (and pop-in events on

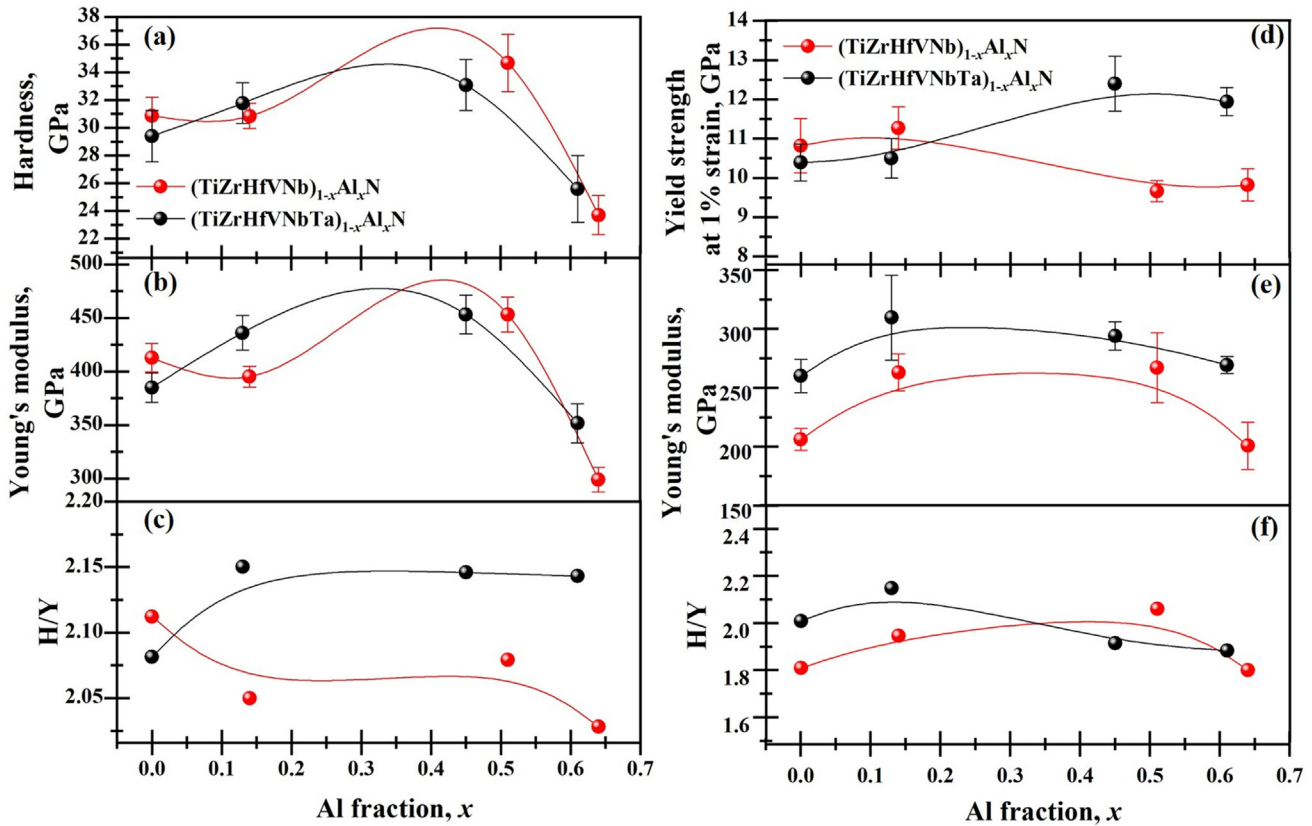


Fig. 8. Mechanical properties of $(\text{TiZrNbHf})_{1-x}\text{Al}_x\text{N}$ ($x = 0, 0.14, 0.51, 0.64$) and $(\text{TiZrNbHfTa})_{1-x}\text{Al}_x\text{N}$ ($x = 0, 0.13, 0.45, 0.61$) thin films measured by means of nanoindentation (a-c) and micro-pillar compression (d-f). The lines are used as a guide for the eye.

load-displacement curves) hinders quantitative calculation of the toughness of the films using well-known analytical approaches [50]. The analytical expression that relates the fracture toughness, K_c , and the length of residual radial cracks whose length (c) must be two times longer than the radius of corresponding impression (a), is given as follows [51]:

$$K_c = \alpha \left(\frac{E}{H} \right)^{0.5} \left(\frac{P}{c_m^{1.5}} \right) \quad (1)$$

where P is the applied indentation load, E and H are the elastic modulus and hardness of the film, respectively, c is the average length of radial cracks, δ is an empirical constant which depends on the geometry of the indenter (0.0319 for cube-corner indenter [50]). In order to perform a relative comparison of the nanoindentation toughness of the films, as a first approximation, the formation of radial cracks can be assumed at an indentation load of 80 mN with the length that satisfy the minimum criterion for a well-defined crack $c = 2a$. Calculation of the K_c of the films following this approximation and based on the measured radius of the impressions (a) shows the increment of the K_c of the single phase films as a function of Al content and significantly lower toughness of the dual-phase films. Although it is a very rough approximation, this is in agreement with SEM observation of plastic flow around the indenter and absence of pop-in events on the load-displacement curves during nanoindentation to the depth that correspond to 90% of the film thickness. The appearance of plastic flow around the indenter and rather similar residual compressive stresses in the films imply better toughness/ductility of single-phase thin films with the highest Al content.

The micro-pillar compression measurements are performed *in situ* in SEM, which provides direct visualization of the deformation mechanism changes and allows to correlate the observed events in the stress-strain curves to the deformation inflicted on the pillars. Engineering stress-strain curves from the micro-pillar load-displacement data are presented in Fig. 10 as function of Al fraction with corresponding post-deformation SEM images. The deformation of all pillars starts with the linear elastic regime. Al-free pillars demonstrate elastic deformation followed by a short-lived plastic regime before catastrophic brittle failure (Fig. 10a,f). Although failure of some pillars has signs of brittleness, their stress-strain curves have a pronounced short plastic region before reaching the failure stress and therefore, the yield strength at 1% strain, Y , is calculated (Fig. 8d). Low- x films demonstrate similar deformation, but immediate catastrophic brittle fracture after elastic deformation. Considering that debris formed after catastrophic failure have the shape of the initial columnar grains, the brittle failure of the pillars of the Al-free and low- x films can be associated with limited dislocation motion in the nanocrystalline materials with high density of grain boundaries. However, the yield strength at 1% strain of these films is very similar and within the experimental error for both hexanary and heptanary HfN thin films, which is in agreement with measured hardness. Noteworthy is that, the single-phase films with highest Al content demonstrate markedly different deformation behavior with more ductile failure. Although being the hardest, these two films demonstrate different stress-strain curves and post deformation state. This is evident as more pronounced compressive ductility of the hexanary film with relatively lower yield strength at 1% strain, whereas the heptanary film has much higher strength, but lower ductility. Interestingly,

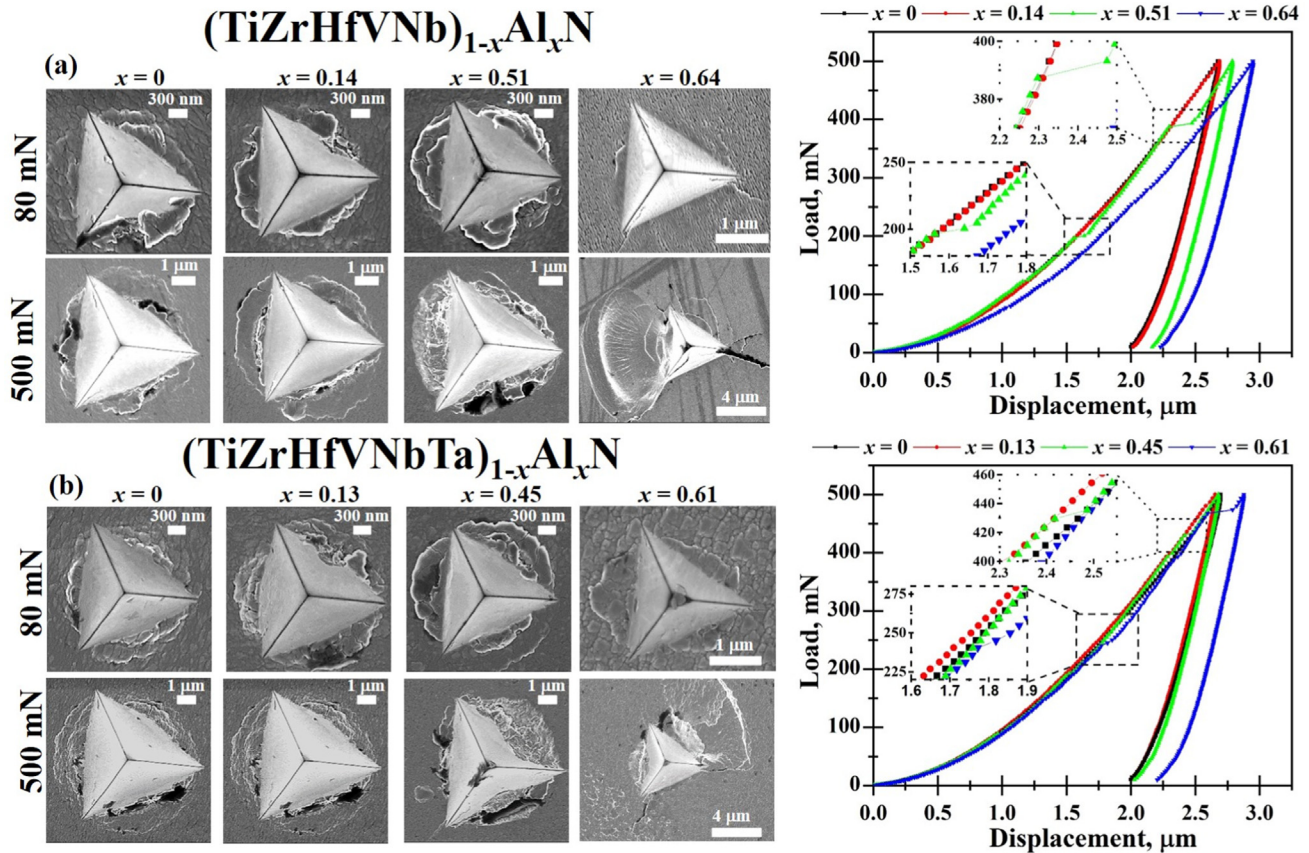


Fig. 9. Nanoindentation fracture toughness results of $(\text{TiZrNbHf})_{1-x}\text{Al}_x\text{N}$ ($x = 0, 0.14, 0.51, 0.64$) (a) and $(\text{TiZrNbHfTa})_{1-x}\text{Al}_x\text{N}$ ($x = 0, 0.13, 0.45, 0.61$) (b) thin films: SEM images of the residual imprints after indentation at 80 mN and 500 mN load, and corresponding load displacement curves (c-d).

the yield strength of dual-phase films follows the same trend. It is worth noting that some films contain pop-ins (strain bursts) before cracking in the stress-strain curves. Considering that pop-ins occur before the appearance of the first crack on the SEM video of compression (see [Supplementary Video 1-8](#)), such events can be associated with a strain hardening and can be a clear indication of plastic deformation in the pillars [52]. It is revealed that the Young's modulus measured by micro-pillar compression (Fig. 8e) is lower than that measured by nanoindentation (Fig. 8b). This can be due to error in pillar height measurement (FIB undercutting), pillar taper and error from the sink-in effect that ultimately all affect the absolute strain measured in micro-pillar compression [53].

To interpret the origin of the strength of single-phase thin films, a classic analysis of the resolved shear stress of a pillar is utilized [54]. The resolved flow strength of the pillar (τ_{sum}) can be contributed by lattice friction (τ^*), Taylor hardening (τ_G), source-controlled strength (τ_S) and grain-boundary strengthening (τ_{h-p}), expressed as:

$$\tau_{\text{sum}} = \sigma m = \tau^* + \tau_G + \tau_S + \tau_{h-p} = \left(1 - \frac{T_t}{T_c}\right) \tau_0^* + \alpha b G \sqrt{\rho} + K G \frac{\ln(\lambda/b)}{\lambda/b} + m K_{h-p} G d^{-1/2} \quad (2)$$

where σ is the flow stress, m the Schmid factor, T_t the test temperature, T_c the critical temperature, τ_0^* the Peierls stress of the active slip system considered, α a constant lying in the range 0.1–1.0, b the Burgers vector, G shear modulus, ρ is dislocation density (10^{15} – 10^{16} $1/\text{m}^2$ for PVD TMNs [55]), K is the source-strength constant of the

order of 0.1, λ average source length (proportional to pillar dimension), and K_{h-p} is the Hall-Petch constant ($12.5 \text{ GPa}/\text{nm}^{-1}$ [56]), d the grain size. Considering that Peierls stress and Hall-Petch constant are not available for HENs, the parameters for the most thoroughly investigated TMN, TiN, are chosen. To make an estimate of the pillar strengths the following constants are set as $K \approx 0.5$, $\lambda \approx D$, $\alpha \approx 0.5$. The diameters of columnar grains of the films estimated by TEM are chosen as the grain size. The micro-pillars of the HEN thin films are composed of a set of strongly textured $\langle 111 \rangle$ and $\langle 001 \rangle$ columnar grains, and thus it is important to consider typical elastic anisotropy of TMNs when calculating the strength of the pillars. The shear modulus of $\langle 111 \rangle$ and $\langle 001 \rangle$ grains is calculated following the rule of mixture of corresponding binary nitrides considering non-isotropic Poisson's ratio [57]. Since the films exhibit fine-fibrous microstructure with $\langle 111 \rangle$ and $\langle 001 \rangle$ oriented columnar grains with diameters of ~ 80 – 100 nm , the Schmid factors available in the literature for the single-crystal TiN for the most probable slip systems for loading along $\langle 111 \rangle$ and $\langle 001 \rangle$ are used. It is experimentally confirmed that TiN has two active slip systems at room temperature $\{111\} \langle 110 \rangle$ ($m = 0.27$) and $\{110\} \langle 110 \rangle$ ($m = 0.5$) in $\langle 111 \rangle$ and $\langle 001 \rangle$ oriented crystals, respectively, with propagation of a partial $a_0/6 \langle 211 \rangle$ and full dislocation $a_0/2 \langle 110 \rangle$, respectively [58,59]. Recent experimental [58] and theoretical [60] studies show that Peierls stress for propagation of a partial dislocation on $\{111\}$ planes is larger ($\tau_{\{111\}\langle 110 \rangle}^* = 2.3 \text{ GPa}$) than that for full dislocation on $\{110\}$ plane ($\tau_{\{110\}\langle 110 \rangle}^* = 1.3$ – 1.4 GPa). Considering this anisotropy and almost equal amount of a set of columnar $\langle 111 \rangle$ and $\langle 001 \rangle$ grains in single-phase films, we determine here the necessary Peierls stress to describe the experimental data. It is worth pointing out that the same fit can be achieved with the

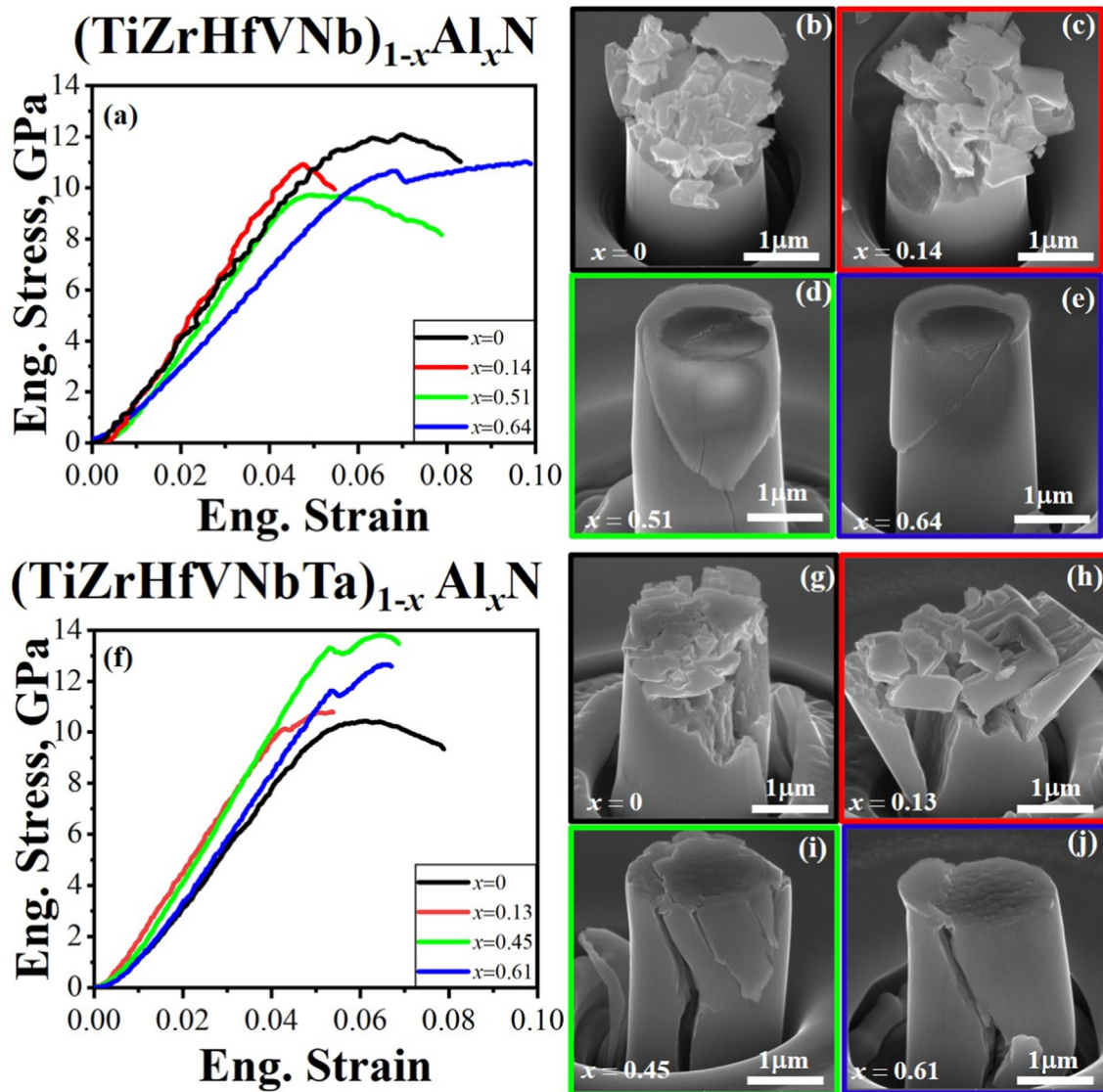


Fig. 10. Representative engineering stress–strain curves derived from compression testing of micro-pillars fabricated by FIB milling of the $(\text{TiZrNbHf})_{1-x}\text{Al}_x\text{N}$ ($x = 0, 0.14, 0.51, 0.64$) (a) and $(\text{TiZrNbHfTa})_{1-x}\text{Al}_x\text{N}$ ($x = 0, 0.13, 0.45, 0.61$) (b) thin films, and corresponding post-compression SEM images.

final variable, the dislocation density in the pillars, but this is unconsidered in our analysis because when the pillar size is much larger than the grain size, the size-effects on strength are determined by grain size. Peierls stress of $\tau^*_{\{111\}\langle 110 \rangle} = 2.6\text{--}2.7$ GPa and $\tau^*_{\{110\}\langle 110 \rangle} = 1.6\text{--}1.7$ GPa for Al-free and low alloyed HEN thin films are deduced from the experimental values. At the same time, the Peierls stresses of $\tau^*_{\{111\}\langle 110 \rangle} = 3.3$ GPa and $\tau^*_{\{110\}\langle 110 \rangle} = 2.6$ GPa are found for the measured values for Al-rich heptanary single-phase film. The grain sizes of the compared films are very similar, as follows from DF-TEM images (Fig. 3 b, k) and Γ_{111} values (Fig. 2d), hence, the Hall-Petch strengthening cannot be responsible for the increase of the yield strength of the Al-rich heptanary single-phase film.

This implies that the increase of Peierls stress is the dominant strengthening mechanism in single-phase HEN thin films. These assumptions are supported by recent theoretical calculations that show that Peierls stress increases when increasing the number of elements in the high-entropy ceramics due to a random interaction of different elements at a dislocation core that ultimately improve the hardness [61]. It is obvious that the yield strength of the dual phase thin films is determined by the *hex* phase in addition to *fcc*

phase and the higher yield strength of the Al-rich dual-phase heptanary HEN thin film than that of corresponding hexanary film can be attributed to a lower fraction of *hex* phase in the former film.

However, in the case of the Al-rich hexanary single phase films no good fit to the experimental data can be obtained using the same approach, which implies that additional mechanisms are active during the pillar deformation. Apart from that, micro-compression results agree very well with indentation results with only the Al-rich hexanary single phase film ranked lower by compression than nanoindentation.

In order to relate hardness and yield strength, it is worth emphasizing that perfectly plastic materials have H/Y of ~ 3 , while brittle ceramic materials can approach H/Y values of 1 [53]. Before determining the H/Y ratio of the HEN films, one should take into account the different stress fields created during compression (uniform uniaxial) and indentation (non-uniform triaxial) and the related impact on the measured mechanical properties. Moreover, we propose to differentiate the impact of the relaxation of compressive residual stresses in the pillar material after FIB milling [62] on measured yield strength and the effect of the confining pressure of the surrounding material of the film under the indenter

tip and the compressive residual stresses in the films on the measured hardness [63]. Therefore, in order to establish a context for relation of yield strength to hardness of the material of the film and the material of the pillar, corresponding hardness/yield strength values are determined by converting yield strength to hardness (and vice versa) values obtained by compression/nanoindentation using an analytical relationship between hardness, H , and yield stress, Y , derived by Vandeperre et al. [64] (Fig. 8c and f). It is evident that Al-free and low- x heptanary pillars behave more plastically than corresponding hexanary pillars (Fig. 8f). The higher H/Y values imply that there is a plastic or dislocation-controlled flow in the pillar during compression. However, the H/Y values of Al-free and low x pillars differ to within ~ 0.15 and cannot provide a background for estimation of plasticity in these materials as Al-free pillars undergo more ductile failure than Al-containing pillars. In contrast, the hexanary Al-rich film that is ranked lower by compression than by indentation demonstrate better plasticity in terms of H/Y than corresponding heptanary alloy also evidenced as more ductile failure at lower stress. At the same time, the H/Y ratio derived from indentation (Fig. 9c) does not show considerable change as a function of Al content in the films with almost similar values for Al-free films and higher values of the heptanary films.

Recent theoretical studies show that there is an energetically favorable formation of $\{111\}$ SFs in fcc-structured TMN domains that are thermodynamically-inclined to crystallize in hexagonal structure [65]. Considering that negative SF energies and structural energy difference between fcc and hex structure are maximized at $VEC \sim 10$ e⁻/f.u. [65] and the fact that the heptanary HEN contains more TMNs whose thermodynamical ground state structure is hexagonal (Supplementary Table 3) then in the hexanary system, the energetic preference to form $\{111\}$ SFs in Al-free films can theoretically promote the observed ductility. The improvement of ductility occurs via assisting slip along the faults (creation of plasticity routes) and stress dissipation as the energy barrier is considerably reduced. Although, as mentioned above, SFs can also effectively impede dislocation motion across the faults, the relative impact of SFs on strength-ductility trade-off in HENs remains open. Another mechanism promoting activation of plastic deformation at the material yield point in TMNs is the formation of a layered electronic structure assisting the activation of the $\{110\}$ $\langle 110 \rangle$ slip system due to full occupation of d- t_{2g} metallic states at VEC 9 e⁻/f.u. upon shearing [66]. Other mechanisms like recently observed modification in atomic coordination triggered at the material yield point of high-entropy carbides with $VEC \sim 9.4$ e⁻/f.u. cannot be excluded to be active in the HENs [67]. Moreover, recent theoretical calculations show that NbN and TaN contribute to minimization of SF energy of $\{111\}$ $\langle 112 \rangle$ slip system in high-entropy nitride systems in addition to $\{110\}$ $\langle 110 \rangle$ and $\{111\}$ $\langle 110 \rangle$ slip systems [68]. Therefore, additional slip systems typical for all fcc TMNs present in the solid solution can be active and contribute to ductility of HENs films [65,69]. It is experimentally observed that more than one slip systems can be active during deformation, for instance, evidenced in TM carbides at room temperature [70].

However, Al-rich pillars with VEC around 8.7 e⁻/f.u. are less thermodynamically inclined to activate slip systems and SF formation via above-described mechanisms. Moreover, due to fully populated strong p (N)-d(Me) bonding states and unoccupied shear-sensitive d-d bonds (Fig. 7d, e), the formation of metallic bonds upon shearing can be rather excluded. This accounts for different intrinsic mechanism responsible for the observed plasticity in these systems. However, the recent density function ab initio molecular dynamic investigation demonstrates that the modifications in the bonding network that become operative in Al-rich TiAlN systems as local structural changes into wurtzite-like tetragonal atomic environments when the elongation overcomes their

yield points, ultimately result in enhanced resistance to fracture and a substantially increased toughness [71]. As the hexanary system is thermodynamically more inclined to fcc-hex phase transformation than heptanary due to higher Al content, the local lattice transformations into wurtzite-like structures during uniaxial strain can dissipate stresses and enhance ductility/plasticity. The observed SFs in the hexanary Al-rich single-phase HEN can be considered as initial faults that did not sufficiently coalesce to form the thermodynamically favoured hexagonal phase but are likely to act as hexagonal phase-formation nuclei when subjected to externally applied uniaxial loads. Additional evidence of the phase transformation toughening of the hexanary Al-rich single-phase pillars is that the post-deformation state (crack pattern) and stress-strain curves of this material is very similar to that of the film containing hex phase. Heptanary film deform in a less ductile manner due to lower Al content and lower driving force to fcc \rightarrow hex phase transformation. The dual-phase pillars due to high content of Al demonstrate lower but comparable yield strength to single-phase films, and plastic deformation is more evident in hexanary HEN pillars. This can be attributed to the formation of SFs in hex phase that can enhance both strength and ductility, in agreement with previous experimental findings of M. Bartosic et al [72] for dual-phase Al-rich TiAlN thin films.

It is worth noting that H/Y ratio derived from nanoindentation does not reflect clear evidence of brittle-ductile behaviour of the films observed during compression as there is no oscillation of H/Y as a function of Al fraction. This may be attributed to triaxial stress fields created during indentation and the plastic zone, where dislocations nucleate, being concentrated below the indenter tip and confined by pressure of the surrounding material that leads to homogeneous dislocation propagation in a small volume and can hence have a less pronounced effect on the load-displacement curves. In contrast, uniaxial stress fields created in the pillar during compression promotes heterogeneous dislocation propagation promoting dislocation-active processes and making them more evident on stress-strain curves because dislocations can nucleate from the free surface of the pillar [75]. However, the pop-in events encountered in load-displacement curves of hexanary thin film with $x = 0.51$ during cube-corner indentation (Fig. 9c,d) and an absence of clear radial cracks on the surface (Fig. 9a,b) might be circumstantial evidence of deformation-induced phase transformation in this film.

5. Conclusions

Hexanary (TiHfNbVZr)_{1-x}Al_xN and heptanary (TiHfNbVZrTa)_{1-x}Al_xN high-entropy nitride thin films with Al content $x = \text{Al}/(\text{TM} + \text{Al})$ varying from ~ 0.13 to ~ 0.64 are synthesised utilizing a hybrid PVD method based on DC and HiPIMS magnetron sputtering. Despite theoretically predicted destabilization of the multi-component NaCl-structured solid solution systems caused by alloying with Al, HEN films exhibit Al solubility limits up to $x \sim 0.51$ – 0.61 and up to $x \sim 0.45$ – 0.64 for the hexanary and heptanary alloy, respectively. The formation of the metastable multi-component solid solution is attributed to a synergistic effect of miscible transition metal nitride pairs in the solution and kinetic constraints created by non-equilibrium growth conditions and Al⁺ subplantation. By alloying with Al the indentation hardness of the films increase from 30.9 ± 1.3 GPa in the Al-free hexanary alloy up to 34.7 ± 2.1 GPa in the hexanary single-phase films with the highest Al content and from 29.4 ± 1.9 GPa in the Al-free heptanary alloy up to 33.1 ± 1.9 GPa in the heptanary single-phase films with the highest Al content. The increment is attributed to severe lattice distortion and strong ionic Metal-N bonding in the Al-rich single-phase films. The formation of dual-phase

microstructure $fcc + hex$ for $x > 0.51$ in hexanary and $x > 0.45$ in heptanary alloys deteriorates both hardness and elastic modulus due to the formation of softer hexagonal phase. Nanoindentation fracture toughness measurements demonstrate a relatively similar toughness of all single-phase films evidenced as a plastic flow around the indenter and absence of clear cracks during indentation up to the depth of 90% of the film thickness. The micro-pillar compression measurements performed *in situ* in an SEM allowed to determine different deformation mechanisms in the pillars depending on the Al fraction. Al-free thin films demonstrate comparable yield strength in the range 10.4–11.4 GPa and plastic deformation before failure that is attributed to several intrinsic electronic-level mechanisms leading to an increment of stacking faults density or activation of slip systems. The high yield strength of Al-free, low x and heptanary single-phase thin films with highest Al content is assigned to synergetic effects of several strengthening mechanisms with lattice friction strengthening being dominant. The hexanary single-phase solid-solution films with $x = 0.51$ demonstrate pronounced plasticity that is attributed to phase transformation toughening.

Based on the presented results it is projected that relaxing maximum entropy criteria opens a vast composition space of non-equimolar high-entropy nitrides, as here, and provides additional space for property tuning that can lead to exploration of new phenomena and properties in high-entropy ceramic materials.

Declaration of Competing Interest

The authors declare that they have no known competing financial interests or personal relationships that could have appeared to influence the work reported in this paper.

Acknowledgments

AVP acknowledges the financial support from the National Science Centre of Poland (SONATINA 2 project, UMO-2018/28/C/ST5/00476), the Foundation for Polish Science (FNP) under START scholarship (START 72.2020), and Polish National Agency for Academic Exchange under the Bekker Programme (PPN/BE K/2019/1/00146/U/00001). AV acknowledges the financial support from the National Science Centre of Poland (SONATINA 2 project, UMO-2018/28/C/ST5/00476). GG, BB, and LH acknowledge the financial support from the Swedish Research Council VR Grant number 2018-03957, 2019-00191 (for accelerator-based ion-technological center in tandem accelerator laboratory in Uppsala University), and 2021-00357, the Swedish Energy Agency under project 51201-1, the Knut and Alice Wallenberg Foundation Scholar Grant KAW2016.0358, and the Carl Tryggers Stiftelse contracts CTS 20:150, CTS 15:219 and CTS 14:431. TEJE acknowledges funding from the European Union's Horizon 2020 research and innovation programme under the Marie Skłodowska-Curie grant agreement No. 840222.

Appendix A. Supplementary data

Supplementary data to this article can be found online at <https://doi.org/10.1016/j.matdes.2022.110798>.

References

- [1] M. Wittmer, M. Wittmer, Properties and microelectronic applications of thin films of refractory metal nitrides Properties and microelectronic applications of thin films of refractory metal nitrides, *J. Vac. Sci. Technol.*, A 3 (1985) 1797, <https://doi.org/10.1116/1.573382>.
- [2] A.P. Serro, C. Completo, R. Colaco, F. dos Santos, C.L. da Silva, J.M.S. Cabral, H. Araújo, E. Pires, B. Saramago, A comparative study of titanium nitrides, TiN, TiNbN and TiCN, as coatings for biomedical applications, *Surf. Coat. Technol.* 203 (24) (2009) 3701–3707, <https://doi.org/10.1016/j.surfcoat.2009.06.010>.
- [3] B. Cantor, I.T.H. Chang, P. Knight, A.J.B. Vincent, Microstructural development in equiatomic multicomponent alloys, *Mater. Sci. Eng., A* 375–377 (2004) 213–218, <https://doi.org/10.1016/j.msea.2003.10.257>.
- [4] B.S. Murty, J.W. Yeh, S. Ranganathan, High-Entropy Alloys (HEAs), Elsevier (2014), <https://doi.org/10.3390/met8020108>.
- [5] C. Oses, C. Toher, S. Curtarolo, High-entropy ceramics, *Nat. Rev. Mater.* 5 (4) (2020) 295–309, <https://doi.org/10.1038/s41578-019-0170-8>.
- [6] J.M. Schneider, How high is the entropy in high entropy ceramics?, *J. Appl. Phys.* 130 (15) (2021) 150903, <https://doi.org/10.1063/5.0062523>.
- [7] E. Lewin, Multi-component and high-entropy nitride coatings—A promising field in need of a novel approach, *J. Appl. Phys.* 127 (16) (2020) 160901, <https://doi.org/10.1063/1.5144154>.
- [8] J. Hou, W. Song, L. Lan, J. Qiao, Surface modification of plasma nitriding on AlxCoCrFeNi high-entropy alloys, *J. Mater. Sci. Technol.* 48 (2020) 140–145, <https://doi.org/10.1016/j.jmst.2020.01.057>.
- [9] H. Kindlund, D.G. Sangiovanni, I. Petrov, J.E. Greene, L. Hultman, A review of the intrinsic ductility and toughness of hard transition-metal nitride alloy thin films, *Thin Solid Films* 688 (2019) 137479, <https://doi.org/10.1016/j.tsf.2019.137479>.
- [10] D.G. Sangiovanni, V. Chirita, L. Hultman, Toughness enhancement in TiAlN-based quaternary alloys, *Thin Solid Films* 520 (11) (2012) 4080–4088, <https://doi.org/10.1016/j.tsf.2012.01.030>.
- [11] K. Kutschej, N. Fateh, P.H. Mayrhofer, M. Kathrein, P. Polcik, C. Mitterer, Comparative study of Ti1–xAlxN coatings alloyed with Hf, Nb, and B, *Surf. Coat. Technol.* 200 (1–4) (2005) 113–117, <https://doi.org/10.1016/j.surfcoat.2005.02.072>.
- [12] G. Greczynski, I. Petrov, J.E. Greene, L. Hultman, Paradigm shift in thin-film growth by magnetron sputtering: From gas-ion to metal-ion irradiation of the growing film, *J. Vac. Sci. Technol., A* 37 (2019), <https://doi.org/10.1116/1.5121226> 060801.
- [13] G. Greczynski, S. Mráz, M. Hans, J. Lu, L. Hultman, J. Schneider, Control over the Phase Formation in Metastable Transition Metal Nitride Thin Films by Tuning the Al+ Subplantation Depth, *Coatings* 9 (1) (2019) 17, <https://doi.org/10.3390/coatings9010017>.
- [14] G. Greczynski, S. Mráz, M. Hans, D. Primetzhofer, J. Lu, L. Hultman, J.M. Schneider, Unprecedented Al supersaturation in single-phase rock salt structure VAlN films by Al+subplantation, *J. Appl. Phys.* 121 (17) (2017) 171907, <https://doi.org/10.1063/1.4977813>.
- [15] K. Kutschej, P.H. Mayrhofer, M. Kathrein, P. Polcik, C. Mitterer, A new low-friction concept for Ti1–xAlxN based coatings in high-temperature applications, *Surf. Coat. Technol.* 188–189 (2004) 358–363, <https://doi.org/10.1016/j.surfcoat.2004.08.022>.
- [16] G. Greczynski, J. Lu, J. Jensen, I. Petrov, J.E. Greene, S. Bolz, W. Köllker, C. Schiffer, O. Lemmer, L. Hultman, Metal versus rare-gas ion irradiation during Ti1–xAlxN film growth by hybrid high power pulsed magnetron/dc magnetron co-sputtering using synchronized pulsed substrate bias, *J. Vac. Sci. Technol., A* 30 (6) (2012) 061504, <https://doi.org/10.1116/1.4750485>.
- [17] B. Bakhit, D. Primetzhofer, E. Pitthan, D. Primetzhofer, E. Pitthan, M.A. Sortica, E. Ntemou, J. Rosen, L. Hultman, I. Petrov, G. Greczynski, Systematic compositional analysis of sputter-deposited boron-containing thin films, *J. Vac. Sci. Technol., A* 39 (2021), <https://doi.org/10.1116/6.0001234> 063408.
- [18] M.P. Seah, Summary of ISO/TC 201 standard: VII ISO 15472 : 2001 - surface chemical analysis - x-ray photoelectron spectrometers - calibration of energy scales, *Surf. Interface Anal.* 31 (2001) 721–723, <https://doi.org/10.1002/sia.1076>.
- [19] G. Greczynski, L. Hultman, X-ray photoelectron spectroscopy: Towards reliable binding energy referencing, *Prog. Mater. Sci.* 107 (2020) 100591, <https://doi.org/10.1016/j.pmatsci.2019.100591>.
- [20] B. Bakhit, D.L.J. Engberg, J. Lu, J. Rosen, H. Högborg, L. Hultman, I. Petrov, J.E. Greene, G. Greczynski, Strategy for simultaneously increasing both hardness and toughness in ZrB2-rich Zr1–xTaxBy thin films, *J. Vac. Sci. Technol., A* 37 (3) (2019) 031506, <https://doi.org/10.1116/1.5093170>.
- [21] H. Zhang, B.E. Schuster, Q. Wei, K.T. Ramesh, The design of accurate micro-compression experiments, *Scr. Mater.* 54 (2) (2006) 181–186, <https://doi.org/10.1016/j.scriptamat.2005.06.043>.
- [22] D. Zagorac, H. Mu, S. Ruehl, J. Zagorac, S. Rehme, Recent developments in the Inorganic Crystal Structure Database : theoretical crystal structure data and related features research papers (2019) 918–925, <https://doi.org/10.1107/S160057671900997X>.
- [23] G. Henkelman, A. Arnaldsson, H. Jónsson, A fast and robust algorithm for Bader decomposition of charge density, *Comput. Mater. Sci.* 36 (3) (2006) 354–360, <https://doi.org/10.1016/j.commatsci.2005.04.010>.
- [24] X. Li, B. Bakhit, M.P. Johansson Jösaar, I. Petrov, L. Hultman, G. Greczynski, Towards energy-efficient physical vapor deposition: Mapping out the effects of W+ energy and concentration on the densification of TiAlWN thin films grown with no external heating, *Surf. Coat. Technol.* 424 (2021) 127639, <https://doi.org/10.1016/j.surfcoat.2021.127639>.
- [25] Y.Y. Tse, D. Babonneau, A. Michel, G. Abadias, Nanometer-scale multilayer coatings combining a soft metallic phase and a hard nitride phase: Study of the interface structure and morphology, *Surf. Coat. Technol.* 180–181 (2004) 470–477, <https://doi.org/10.1016/j.surfcoat.2003.10.139>.
- [26] M. to Baben, M. Hans, D. Primetzhofer, S. Evertz, H. Ruess, J.M. Schneider, Unprecedented thermal stability of inherently metastable titanium aluminum

- nitride by point defect engineering, *Mater. Res. Lett.* 5 (3) (2017) 158–169, <https://doi.org/10.1080/21663831.2016.1233914>.
- [27] G. Greczynski, I. Zhirkov, I. Petrov, J.E. Greene, J. Rosen, Time evolution of ion fluxes incident at the substrate plane during reactive high-power impulse magnetron sputtering of groups IVb and Vb transition metals in Ar / N₂ Time evolution of ion fluxes incident at the substrate plane during reactive high-power, *J. Vac. Sci. Technol.*, A 36 (2) (2018) 020602, <https://doi.org/10.1116/1.5016241>.
- [28] F. Meng, W. Zhang, Z. Zhou, R. Sheng, A.-P. Chuang, C. Wu, H. Huang, S. Zhang, H. Zhang, L. Zhu, L. Jiang, P.K. Liaw, S. Chen, Y. Tong, Charge transfer effect on local lattice distortion in a HfNbTiZr high entropy alloy, *Scr. Mater.* 203 (2021) 114104, <https://doi.org/10.1016/j.scriptamat.2021.114104>.
- [29] W.-C. Chen, Y.-R. Lin, X.-J. Guo, S.-T. Wu, Heteroepitaxial TiN of very low mosaic spread on Al₂O₃, *Japanese J. Appl. Physics, Part 1 Regul. Pap. Short Notes Rev. Pap.* 42 (Part 1, No. 1) (2003) 208–212, <https://doi.org/10.1143/JJAP.42.208>.
- [30] H. Zaid, K. Tanaka, M. Liao, M.S. Goorsky, S. Kodambaka, H. Kindlund, Self-Organized Growth of 111-Oriented (VNBaMoW)N Nanorods on MgO(001), *Nano Lett.* 21 (1) (2021) 577–582, <https://doi.org/10.1021/acs.nanolett.0c04061>, <https://doi.org/10.1021/acs.nanolett.0c04061.s001>.
- [31] C. Tholander, B. Alling, F. Tasnadi, J.E. Greene, L. Hultman, Effect of Al substitution on Ti, Al, and N adatom dynamics on TiN(001), (011), and (111) surfaces, *Surf. Sci.* 630 (2014) 28–40, <https://doi.org/10.1016/j.susc.2014.06.010>.
- [32] M. Stoehr, C.S. Shin, I. Petrov, J.E. Greene, Raman scattering from TiNx (0.67 < x < 1.00) single crystals grown on MgO(001), *J. Appl. Phys.* 110 (2011), <https://doi.org/10.1063/1.3651381>.
- [33] K. Schwarz, Band structure and chemical bonding in transition metal carbides and nitrides, *Crit. Rev. Solid State Mater. Sci.* 13 (3) (1987) 211–257, <https://doi.org/10.1080/10408438708242178>.
- [34] G. Greczynski, D. Primetzhofer, J. Lu, L. Hultman, Core-level spectra and binding energies of transition metal nitrides by non-destructive x-ray photoelectron spectroscopy through capping layers, *Appl. Surf. Sci.* 396 (2017) 347–358, <https://doi.org/10.1016/j.apsusc.2016.10.152>.
- [35] P.S. Bagus, A. Wieckowski, H. Freund, The contribution of lattice strain to core-level binding energy shifts in metal nanoparticles: Generality and origin of the shifts, *Comput. Theor. Chem.* 987 (2012) 22–24, <https://doi.org/10.1016/j.comptc.2011.06.028>.
- [36] N. Ghafoor, I. Petrov, D. Holec, G. Greczynski, J. Palisaitis, P.O.A. Persson, L. Hultman, J. Birch, Self-structuring in Zr 1-x Al x N films as a function of composition and growth temperature, *Sci. Rep.* (2018) 1–17, <https://doi.org/10.1038/s41598-018-34279-w>.
- [37] Z.T.Y. Liu, B.P. Burton, S.V. Khare, D. Gall, First-principles phase diagram calculations for the rocksalt-structure quaternary systems TiN-ZrN, TiN-HfN and ZrN-HfN, *J. Phys.: Condens. Matter* 29 (3) (2017) 035401, <https://doi.org/10.1088/0953-8984/29/3/035401>.
- [38] A.A. Bagdasaryan, A.V. Pshyk, L.E. Coy, P. Konarski, M. Misnik, V.I. Ivashchenko, M. Kempinski, N.R. Mediuik, A.D. Pogrebniak, V.M. Beresnev, S. Jurga, A new type of (TiZrNbTaHf)N/MoN nanocomposite coating: Microstructure and properties depending on energy of incident ions, *Compos. Part B Eng.* 146 (2018) 132–144.
- [39] P. Duwez, F. Odell, Phase Relationships in the Binary Systems of Nitrides and Carbides of Zirconium, Columbium, Titanium, and Vanadium, *J. Electrochem. Soc.* 97 (10) (1950) 299, <https://doi.org/10.1149/1.2777885>.
- [40] P. Ou, J. Wang, S. Shang, L. Chen, Y. Du, Z.K. Liu, F. Zheng, A first-principles study of structure, elasticity and thermal decomposition of Ti1-xTMxN alloys (TM = Y, Zr, Nb, Hf, and Ta), *Surf. Coat. Technol.* 264 (2015) 41–48, <https://doi.org/10.1016/j.surfcoat.2015.01.024>.
- [41] G. Abadias, V.I. Ivashchenko, L. Belliard, P.h. Djemia, Structure, phase stability and elastic properties in the Ti1-xZr_xN thin-film system: Experimental and computational studies, *Acta Mater.* 60 (15) (2012) 5601–5614, <https://doi.org/10.1016/j.actamat.2012.07.014>.
- [42] A. Kretschmer, D. Holec, K. Yalamanchili, H. Rudigier, M. Hans, J.M. Schneider, P.H. Mayrhofer, Strain-stabilized Al-containing high-entropy sublattice nitrides, *Acta Mater.* 224 (2022) 117483, <https://doi.org/10.1016/j.actamat.2021.117483>.
- [43] Z.-J. Liu, P.W. Shum, Y.G. Shen, Hardening mechanisms of nanocrystalline Ti-Al-N solid solution films, *Thin Solid Films* 468 (1–2) (2004) 161–166, <https://doi.org/10.1016/j.tsf.2004.05.087>.
- [44] S.-H. Jhi, J. Ihm, S.G. Louie, M.L. Cohen, Electronic mechanism of hardness enhancement in transition-metal carbonitrides, *Nature* 399 (6732) (1999) 132–134, <https://doi.org/10.1038/20148>.
- [45] K. Balasubramanian, S.V. Khare, D. Gall, Valence electron concentration as an indicator for mechanical properties in rocksalt structure nitrides, carbides and carbonitrides, *Acta Mater.* 152 (2018) 175–185, <https://doi.org/10.1016/j.actamat.2018.04.033>.
- [46] H.W. Hugosson, U. Jansson, Borje Johansson, O. Eriksson, Restricting Dislocation Movement in Transition Metal Carbides by Phase Stability Tuning, *Science* 293 (5539) (2001) 2434–2437.
- [47] Y. Tang, D. Zhang, R. Liu, D. Li, Designing high-entropy ceramics via incorporation of the bond-mechanical behavior correlation with the machine-learning methodology, *Cell Reports Phys. Sci.* 2 (11) (2021) 100640, <https://doi.org/10.1016/j.xcrp.2021.100640>.
- [48] P.-L. Larsson, A. E. Giannakopoulos, Tensile stresses and their implication to cracking at pyramidal indentation of pressure-sensitive hard metals and ceramics, *Mater. Sci. Eng., A* 254 (1–2) (1998) 268–281.
- [49] K.A. Rzepiejewska-Malyska, W.M. Mook, M. Parlinska-Wojtan, J. Hejduk, J. Michler, In situ scanning electron microscopy indentation studies on multilayer nitride films: Methodology and deformation mechanisms, *J. Mater. Res.* 24 (3) (2009) 1208–1221, <https://doi.org/10.1557/jmr.2009.0139>.
- [50] S. Zhang, D. Sun, Y. Fu, H. Du, Toughness measurement of thin films: A critical review, *Surf. Coat. Technol.* 198 (1–3) (2005) 74–84, <https://doi.org/10.1016/j.surfcoat.2004.10.021>.
- [51] B.R. Lawn, A.G. Evans, D.B. Marshall, Elastic / Plastic Indentation Damage in Ceramics: The MedialRadial Crack System, *J. Am. Ceram. Soc.* 63 (1980) 574–581, <http://ieeexplore.ieee.org/document/1382345/>.
- [52] I. El Azhari, J. Garcia, M. Zamanzade, F. Soldera, C. Pauly, L. Llanes, F. Mücklich, Investigations on micro-mechanical properties of polycrystalline Ti(C, N) and Zr(C, N) coatings, *Acta Mater.* 149 (2018) 364–376, <https://doi.org/10.1016/j.actamat.2018.02.053>.
- [53] J.M. Wheeler, R. Raghavan, V. Chawla, M. Morstein, J. Michler, Deformation of Hard Coatings at Elevated Temperatures, *Surf. Coat. Technol.* 254 (2014) 382–387, <https://doi.org/10.1016/j.surfcoat.2014.06.048>.
- [54] Y. Zou, H. Ma, R. Spolenak, Ultrastrong ductile and stable high-entropy alloys at small scales, *Nat. Commun.* 6 (2015) 1–8, <https://doi.org/10.1038/ncomms8748>.
- [55] Z. Zhang, A. Ghasemi, N. Koutná, Z. Xu, T. Grünstäudl, K. Song, D. Holec, Y. He, P.H. Mayrhofer, M. Bartosik, Correlating point defects with mechanical properties in nanocrystalline TiN thin films, *Mater. Des.* 207 (2021) 109844, <https://doi.org/10.1016/j.matdes.2021.109844>.
- [56] H. Jia, X. Liu, Z. Li, S. Sun, M. Li, The effect of grain size on the deformation mechanisms and mechanical properties of polycrystalline TiN: A molecular dynamics study, *Comput. Mater. Sci.* 143 (2018) 189–194, <https://doi.org/10.1016/j.commatsci.2017.10.054>.
- [57] A.B. Mei, R.B. Wilson, D. Li, D.G. Cahill, A. Rockett, J. Birch, L. Hultman, J.E. Greene, I. Petrov, Elastic constants, Poisson ratios, and the elastic anisotropy of VN(001), (011), and (111) epitaxial layers grown by reactive magnetron sputter deposition, *J. Appl. Phys.* 115 (21) (2014) 214908, <https://doi.org/10.1063/1.4881817>.
- [58] N. Li, S.K. Yadav, X. Liu, J. Wang, R.G. Hoagland, N. Mara, A. Misra, Quantification of dislocation nucleation stress in TiN through high-resolution in situ indentation experiments and first principles calculations, *Sci. Rep.* 5 (2015) 15813, <https://doi.org/10.1038/srep15813>.
- [59] M. Oden, H. Ljungcrantz, L. Hultman, Characterization of the induced plastic zone in a single crystal TiN (001) film by nanoindentation and transmission electron microscopy, *J. Mater. Res.* 12 (1997) 2134.
- [60] S.K. Yadav, R. Ramprasad, A. Misra, X. Liu, Core structure and Peierls stress of edge and screw dislocations in TiN: A density functional theory study, *Acta Mater.* 74 (2014) 268–277, <https://doi.org/10.1016/j.actamat.2014.04.047>.
- [61] Y. Wang, T. Csanádi, H. Zhang, J. Duszka, M.J. Reece, R.-Z. Zhang, Enhanced Hardness in High-Entropy Carbides through Atomic Randomness, *Adv. Theory Simulations* 3 (9) (2020) 2000111, <https://doi.org/10.1002/adts.v3.910.1002/adts.202000111>.
- [62] M. Sebastiani, E. Bemporad, F. Carassiti, N. Schwarzer, Residual stress measurement at the micrometer scale: focused ion beam (FIB) milling and nanoindentation testing, *Phil. Mag.* 91 (2011) 1121–1136, <https://doi.org/10.1080/14786431003800883>.
- [63] L. Karlsson, L. Hultman, J. Sundgren, Influence of residual stresses on the mechanical properties of evaporation, *Thin Solid Films* 371 (2000) 167–177.
- [64] L.J. Van der Perre, F. Giuliani, W.J. Clegg, Effect of elastic surface deformation on the relation between hardness and yield strength, *J. Mater. Res.* 19 (12) (2004) 3704–3714, <https://doi.org/10.1557/JMR.2004.0473>.
- [65] H. Yu, M. Bahadori, G.B. Thompson, C.R. Weinberger, Understanding dislocation slip in stoichiometric rocksalt transition metal carbides and nitrides, *J. Mater. Sci.* 52 (11) (2017) 6235–6248, <https://doi.org/10.1007/s10853-017-0857-4>.
- [66] D.G. Sangiovanni, L. Hultman, V. Chirita, Supertoughening in B1 transition metal nitride alloys by increased valence electron concentration, *Acta Mater.* 59 (5) (2011) 2121–2134, <https://doi.org/10.1016/j.actamat.2010.12.013>.
- [67] D.G. Sangiovanni, W. Mellor, T. Harrington, K. Kaufmann, K. Vecchio, Enhancing plasticity in high-entropy refractory ceramics via tailoring valence electron concentration, *Mater. Des.* 209 (2021) 109932, <https://doi.org/10.1016/j.matdes.2021.109932>.
- [68] H. Huang, L. Shao, H. Liu, Stacking fault energies of high-entropy nitrides from first-principles calculations, *Solid State Commun.* 327 (2021) 114210, <https://doi.org/10.1016/j.ssc.2021.114210>.
- [69] H. Ljungcrantz, M. Odén, L. Hultman, J.E. Greene, J.-E. Sundgren, Nanoindentation studies of singlecrystal (001), (011), and (111) oriented TiN layers on MgO, *J. Appl. Phys.* 80 (12) (1996) 6725–6733, <https://doi.org/10.1063/1.363799>.
- [70] S. Kiani, J.-M. Yang, S. Kodambaka, D.J. Green, Nanomechanics of Refractory Transition-Metal Carbides: A Path to Discovering Plasticity in Hard Ceramics, *Nanomechanics of Refractory Transition-Metal Carbides: A Path to Discovering Plasticity in Hard Ceramics* 98 (8) (2015) 2313–2323.
- [71] D.G. Sangiovanni, F. Tasnádi, L.J.S. Johnson, M. Odén, I.A. Abrikosov, Strength, transformation toughening, and fracture dynamics of rocksalt-structure Ti1-xAl x (0<x≤0.75) alloys, *Phys. Rev. Mater.* 4 (2020) 1–12, <https://doi.org/10.1103/PhysRevMaterials.4.033605>.
- [72] M. Bartosik, C. Rumeau, R. Hahn, Z.L. Zhang, P.H. Mayrhofer, Fracture toughness and structural evolution in the TiAlN system upon annealing, *Sci. Rep.* (2017) 1–9, <https://doi.org/10.1038/s41598-017-16751-1>.